# Journal of Materials Chemistry A



### **REVIEW**

View Article Online
View Journal | View Issue



Cite this: J. Mater. Chem. A, 2020, 8, 8783

# The coupling of experiments with density functional theory in the studies of the electrochemical hydrogen evolution reaction

Mingpeng Chen,<sup>a</sup> Tyler J. Smart,<sup>b</sup> Shanwen Wang,<sup>a</sup> Tianyi Kou, <sup>b</sup> Dun Lin,<sup>a</sup> Yuan Ping <sup>b</sup> \*<sup>a</sup> and Yat Li <sup>b</sup> \*<sup>a</sup>

The hydrogen evolution reaction (HER) is the cathodic reaction of water electrolysis, which is a cleaner and more sustainable approach to produce hydrogen gas compared to the conventional steam reforming method. Electrocatalysts are essential to lower the overpotential of the HER and, thus, the overall energy cost of water electrolysis. The search for high performance HER catalysts has been facilitated by coupling experiments with first principles calculation, e.g., density functional theory (DFT). This article will first review the factors determining the performance of HER electrocatalysts. Then, we will discuss the power of coupling experiments with DFT in obtaining insights into the fundamentals of the HER, including explaining experimental results and revealing reaction mechanisms, and facilitating the development of new HER electrocatalysts. The last section of this review focuses on the limitations and progress of coupling experiments with DFT from three perspectives: experimental measurements, characterization and DFT simulation. Finally, we share some opinions about how to better couple experiments with DFT.

Received 4th March 2020 Accepted 14th April 2020

DOI: 10.1039/d0ta02549f

rsc.li/materials-a

### 1. Introduction

Hydrogen gas is one of the most important chemicals, which has been widely used for petroleum refining,<sup>1,2</sup> ammonia production,<sup>3,4</sup> fuel cells,<sup>5,6</sup> *etc.* The demand for hydrogen increases exponentially with the increasing global population. To date, steam reforming of natural gas is still the most commonly used industrial method to produce hydrogen gas.<sup>7</sup>

<sup>&</sup>lt;sup>b</sup>Department of Physics, University of California Santa Cruz, 1156 High Street, Santa Cruz, California, 95064, USA



Mingpeng Chen received his bachelor's degree in Materials Science and Engineering from Tianjin University in 2017. Currently, he is a 3<sup>rd</sup>-year graduate student in Prof. Yat Li's group in the Department of Chemistry and Biochemistry at the University of California, Santa Cruz. He is also learning simulation with Prof. Yuan Ping in the same department. His research focuses on electro-

catalysis (such as the hydrogen evolution reduction, oxygen reduction reaction, nitrogen reduction reaction, etc.), DFT calculation and how to better couple DFT calculation with experimental measurements.



Tyler J. Smart received his B.S. degree in physics with a minor in mathematics from Humboldt State University in 2016 and his M.S. degree in physics from the University of California, Santa Cruz in 2018. Currently he is a Ph.D. candidate of physics under the supervision of Prof. Yuan Ping at the University of California, Santa Cruz. His research focus includes the development and application of

first-principles methods for studying polaron formation and transport in transition metal oxides for energy conversion, as well as the defect, spin, and excited state properties of 2D materials for quantum information science.

<sup>&</sup>lt;sup>a</sup>Department of Chemistry and Biochemistry, University of California Santa Cruz, 1156 High Street, Santa Cruz, California, 95064, USA. E-mail: yuanping@ucsc.edu; yatli@

However, the process not only uses non-renewable energy sources but also produces a large amount of carbon dioxide. Water electrolysis is an alternative and more sustainable approach to produce hydrogen gas. If water electrolysis is powered by renewable energy sources such as solar energy, wind energy, etc., then the carbon footprint for hydrogen generation can be further reduced. The hydrogen evolution reaction (HER) is the cathodic reaction of water electrolysis. A highly efficient HER electrocatalyst is essential to decrease the overpotential of the HER and, thus, the overall energy cost of water electrolysis. Platinum (Pt) is known to be the most efficient electrocatalyst for the HER.8 However, the scarcity and high cost of Pt limit its large scale applications. Replacing platinum with earthabundant, inexpensive and highly efficient electrocatalysts has been an outstanding challenge in the field. Fortunately, the search for such electrocatalysts can be facilitated by coupling experiments with first principles calculations, e.g. density functional theory (DFT).9

DFT has become a popular method to investigate the properties of molecular and solid-state materials because of the following reasons: (1) it is able to deal with many-body problems with a relatively economical computational cost compared to other high-cost theories such as random-phase approximation, Møller–Plesset perturbation theory, the coupled-cluster singles and doubles method, quantum Monte Carlo calculation, *etc.* (2) Its accuracy has been improved significantly in the past several decades by using better functionals to a level that is sufficient to explain or predict the properties of interested materials. (3) As shown in Fig. 1, the computational capability worldwide in the past 30 years has an exponential increase, which makes it possible to use DFT to calculate larger and more complicated systems. (6-19)

In this review, we will focus on the accomplishments and challenges of the coupling between experiments and DFT. We will start with the discussion on important factors for determining the performance of HER electrocatalysts. The first factor

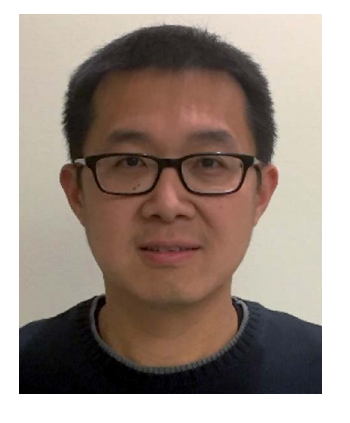
is the thermodynamic adsorption of intermediate H. There are many pathways to manipulate this factor, strategies of heteroatom doping, vacancy engineering and strain engineering are discussed in the review.20-22 The kinetics of H2O dissociation are the second factor, and strategies of orbital engineering and heterogeneous interface construction are discussed.<sup>23,24</sup> The third one is the thermodynamic adsorption of OH<sup>-</sup>, which plays an important role in refreshing the active sites and tuning the energy barrier of H2O dissociation.25 Conductivity of the electrode and the charge transfer between the electrode and electrolyte are two other factors, and they are often coupled with each other and it's usually difficult to distinguish their individual contribution.<sup>26,27</sup> The former consists of three parts: the conductivity of the substrate and catalyst, as well as the electric contact between them, while the latter is governed by a lot of factors such as the potential, surface area, conductivity of the electrode/electrolyte, etc. Besides, the bubble effect cannot be neglected and it becomes significant at a large current. Two methods for facilitating the detachment of bubbles, creating nanostructures and making the electrode surface superaerophobic, are discussed in this review.28,29 Last but not least, we review the stability of electrocatalysts, where different degradation mechanisms are discussed. 30,31 Suggestions on how to improve the stability of electrocatalysts are also provided.

The second section focuses on the accomplishments of coupling experiments with DFT, which are summarized from two perspectives. First, it helps to gain insights into the fundamentals of the HER, including explaining anomalous experimental phenomena such as the pH dependence of H binding energy on a metal surface<sup>32</sup> and predicting reaction mechanisms of the HER on different surfaces, <sup>33-35</sup> which are still hard to study experimentally. Second, it facilitates the development of new HER electrocatalysts such as transition metal dichalcogenides (TMDs), carbon-based materials, single-atom catalysts (SACs) and MXenes. <sup>36-39</sup> For instance, the study of MoS<sub>2</sub> is the earliest demonstration of how DFT helps the search



Yuan Ping received her B.Sc. degree in chemical physics from the University of Science and Technology of China, China, in 2007 and her Ph.D. in theoretical materials chemistry from the University of California, Davis in 2013. She was a materials postdoctoral fellow in the DOE energy hub-JCAP at the California Institute of Technology from 2013 to 2016. In the summer of 2016, she joined the

faculty at the University of California, Santa Cruz as an assistant professor. Ping's research interests focus on first-principles methodology development on excited-state and spin dynamics for solids and nanostructures, and their applications in quantum information science and energy conversion.



Dr Yat Li is a full professor of chemistry and biochemistry at the University of California, Santa Cruz. He received his B.Sc. (1999) and Ph.D. (2002) degrees in Chemistry from The University of Hong Kong. In 2003, he received a Croucher Foundation postdoctoral fellowship to work with Prof. Charles M. Lieber at Harvard University. He joined the University of California, Santa

Cruz as an assistant professor in 2007. His research focuses on the rational design and synthesis of low-dimensional materials, understanding their chemical and physical properties, and realizing their potential applications in catalysis, energy conversion and storage.

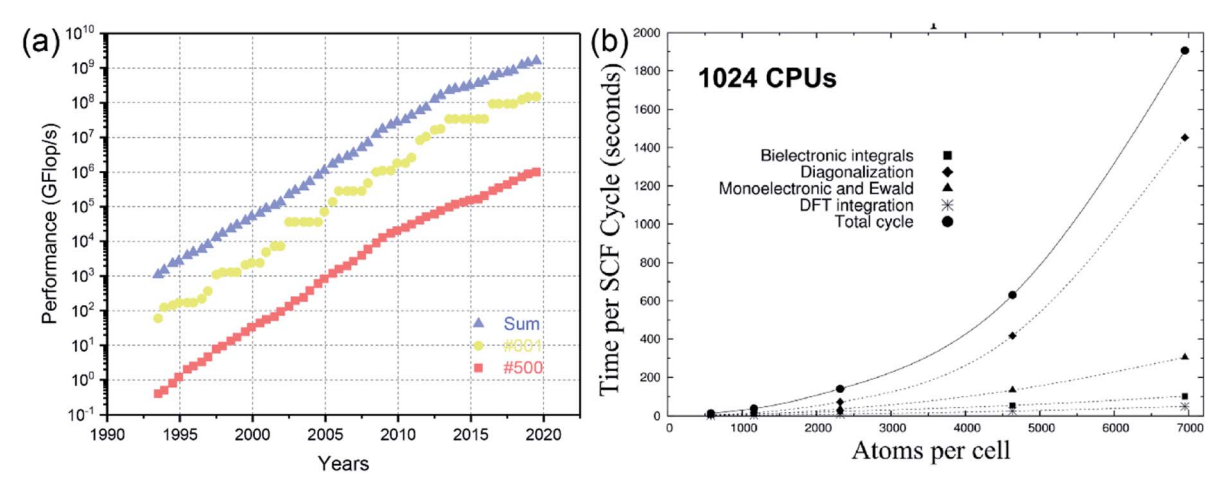


Fig. 1 Computational capability development and computation time scale with the number of atoms per cell. (a) The y-axis (flop per s) in (a) indicates floating point operations per second, which is a metric to evaluate the computer performance. 16 "#001" means the fastest supercomputer in the world, "#500" means the 500th fastest supercomputer in the world and "Sum" means the summation computational capability of the top 500 supercomputers. (b) Wall-clock time (in seconds) of a SCF cycle run in parallel over 1024 processors for MCM-41 supercells of increasing size with the hybrid B3LYP functional. The time required by the main computational tasks in each SCF cycle is also separately reported. (a) Reproduced from ref. 16, copyright 2019, with permission from TOP 500 website; (b) reprinted from ref. 18, copyright 2017, with permission from American Chemical Society.

for promising HER electrocatalysts by using the Gibbs free energy of hydrogen adsorption as the descriptor.<sup>36</sup> Since then, a series of other TMDs were also found to have similar attractive Gibbs free energy of hydrogen adsorption values to MoS<sub>2</sub>, which expanded the scope from one material to one class of materials. Although pristine MoS2 shows a decent HER activity, it is still not comparable to that of Pt. The reasons include the poor conductivity, low density of active edge sites and low activity of largely exposed basal planes of 2H phase MoS2. The corresponding strategies of utilizing 1T metallic phase MoS2, maximizing the number of edge sites and activating the inert basal planes of 2H phase MoS<sub>2</sub> were developed to further boost the activity of MoS2, trying to make it comparable to that of Pt. 40-42 DFT also contributed to the development of carbon-based HER catalysts. Carbon-based materials are attractive because of their low cost, high abundance, and high corrosion resistance. However, a pristine carbon-based material is known to be inert for catalyzing the HER. Different approaches have been employed to engineer carbon-based materials' electronic structures and increase their activities. Among them, doping was found to be one of the most effective methods.37 Although many heteroatoms (e.g., B, N, O, P, and S) have been demonstrated to be useful in boosting the HER activity of carbon, it is still challenging to understand the possible synergistic effect between dopants. DFT calculation can serve as an efficient tool to gain more insights into the interaction between different dopants. SACs are another emerging class of materials for catalyzing the HER. Different from metal bulk or nanostructures, where metal atoms stack with each other and form crystal structures, single metal atoms in SACs are distributed and confined in the substrate such as carbon-based materials or transition metal oxides. People are interested in SACs because they can achieve the 100% utilization of metallic atoms and minimize metal loading, which is important for practical

application, especially for noble metal-based catalysts. For SACs, a challenge is to find suitable dopants for a specific substrate. DFT can help to simplify and accelerate this search process. Instead of testing different dopants experimentally, DFT screening is a more efficient and cheaper method to search for the correct dopants for a specific substrate. 43 MXenes, a new class of two-dimensional materials, were also reported to show promising HER performance recently.39 DFT calculation was used to systematically study a series of MXenes and it was found that they are all conductive under standard conditions and can possess a favorable H adsorption activity when the surface is terminated with suitable groups.44 These computational studies motivated and guided more experimental efforts on MXenes.

There are also a number of unaddressed issues and challenges for coupling experiments with DFT. We discuss these challenges from three perspectives: experimental measurements, characterization and DFT simulation. In the subsection of experimental measurements, the significance of scan rates, reactant diffusion, bubble management, and intrinsic activity comparison is highlighted. The determination of an accurate ECSA is important for comparing the intrinsic activity of different catalysts. Different methods for measuring the ECSA are summarized and compared.45 Characterization provides critical structural information to build models for DFT calculation. The characterization subsection presents the recent advancement of in situ/operando techniques and discusses some new discoveries made by using these techniques. For example, Deng et al. employed operando Raman spectroscopy to study amorphous MoS<sub>x</sub> for the HER and proved that S sites are the active HER sites.46 From the perspective of DFT simulation, there are two major challenges. One is the fundamental limitation of the DFT methodology, while the other is the simulation of the interface between the electrolyte and electrified electrode. Although DFT achieves a good balance between

computation costs and accuracy, this method has issues of inaccurate electron correlation, zero temperature calculation, entropy approximation, etc. The issue of inaccurate electron correlation is more obvious when it comes to strongly correlated systems such as many transition metal oxides. 47 For the simulation of the interface between the electrolyte and electrified electrode, we discuss the discrepancy between the current computation environment and the real working environment, including (1) potential, (2) solvent, (3) solute and (4) pH. The widely used constant charge scheme cannot correctly simulate the effect of potential on the reaction pathway since potential only affects the energy of electrochemical steps in this scheme. 48 In contrast, the constant potential scheme is able to capture the effect of potential on non-electrochemical steps correctly. For example, Ping et al. employed the constant potential scheme to study the reaction mechanism of the oxygen evolution reaction (OER) on IrO2 and showed that the non-electrochemical steps under constant charge conditions can be strongly electrochemically dependent under realistic constant potential conditions.49 There are two general approaches to include the effect of solvent, explicit solvent models and implicit solvent models. Although explicit solvent models give more insights into the interaction between solvents and solutes, 32,50-52 they are computationally more expensive. Implicit solvent models, on the other hand, replace explicit solvent molecules with polarizable dielectric media and are relatively computationally more economical and can provide an average description of the overall solvent behavior. There are some new implicit solvent models developed recently such as the charge-asymmetric nonlocally determined local-electric (CANDLE) solvent model, which enables an explicit treatment of charge asymmetric solvents.53 The effect of solutes also has to be taken into account, and it has been demonstrated by Pham et al. that it can be quantitatively described by using first principles molecular dynamics (MD) calculations and electronic structure calculations with dielectric dependent hybrid functionals.54 The pH effect is complicated; however, it is important to be included in the computation environment. One easy approach to simulate the pH effect is to convert the pH effect to the potential effect by using the Nernst equation, but it cannot fully describe the pH effect.32 The pH effect can also be depicted by correlating the pH to the chemical potential of isolated ions. Ambrosio et al. employed this method to study the pH dependence on the BiVO<sub>4</sub> (010) surface and found that protons, H<sub>2</sub>O molecules, and hydroxyl groups are the dominant groups in strongly acidic media, media with pH ranging from 2 to 8 and pH larger than 8.2, respectively.55 In the last section, we also proposed some strategies to improve the coupling between experiments and DFT calculations.

# 2. The key factors for determining the performance of HER electrocatalysts

A number of important factors (Fig. 2) that determine the performance of HER electrocatalysts are discussed in this section. The discussion of each factor starts with a general



Fig. 2 Important factors that determine the performance of HER electrocatalysts.

background, followed by representative examples to illustrate how this factor affects the performance of HER electrocatalysts. Improving the overpotential of HER electrocatalysts is one of the most important goals in the community. Unfortunately, there is no simple answer for the question of how to improve the HER overpotential down to the level of Pt. Different materials have different intrinsic catalytic activities for each step in the HER, so a distinct approach is needed for each catalyst. Despite the complexity of the question, there are some general approaches to improve the activity of HER electrocatalysts such as improving the conductivity, increasing the number of active sites and enhancing the intrinsic activity of each active site. For example, MoS2 is a representative HER material.36 Its activity is known to be hindered by the poor conductivity. Therefore, using 1T metallic phase MoS2 can increase its activity.40 Jaramillo et al. found that the edges of 2H semiconducting phase MoS<sub>2</sub> are active sites, 42 so the structural engineering approach has been employed to maximize the number of exposed edge sites.56,57 In addition, vacancy and strain engineering have also been employed to activate the inert 2H MoS<sub>2</sub> basal plane. 41 The orbital engineering approach has been used to improve the activity of MoS2 in alkaline medium.58 For other materials, for example, pristine carbon-based materials are known to be inert for catalyzing the HER. Strategies such as heteroatom doping have been used to boost its activity. 3-Dimensional graphene structures achieved a current density of 10 mA cm<sup>-2</sup> at a small overpotential of 107 mV.59 Transition metal oxides such as NiO are known to be good materials for H2O adsorption and dissociation but lack active H adsorption sites. By creating more favorable H adsorption sites on the surface via doping, its activity has been significantly improved to close to the level of Pt, with an ultrasmall overpotential of 27 eV at a current density of 10 mA cm<sup>-2</sup>.60 These examples suggest that specific strategies are required to tackle specific limitations in different HER materials. A general approach is to first understand the catalytic mechanism of the HER catalyst, identify the questions needed to be addressed, and then develop the right strategies through the combination of computational and experimental efforts.

### 2.1. Thermodynamic adsorption of intermediate H

The HER consists of two steps. 61 The first step is called the Volmer step, in which intermediate H is generated. For the second step, there are two possible mechanistic pathways: Heyrovsky step and Tafel step. In the Heyrovsky step, intermediate H reacts with another proton or H<sub>2</sub>O molecule to generate an H2 molecule. Alternatively, two intermediate H combine to form a H<sub>2</sub> molecule in the Tafel step.<sup>62,63</sup> Depending on the reaction media, the reaction mechanism would be different. In acidic media, the reactions are:

Volmer step: \* + H<sup>+</sup> + e<sup>-</sup> 
$$\rightarrow$$
 \*H (1)

Heyrovsky step: 
$$*H + H^+ + e^- \rightarrow *H_2$$
 (2)

Tafel step: 
$$*H + *H \rightarrow *H_2$$
 (3)

Among which, \* is the active site on the surface. In alkaline media, an additional H<sub>2</sub>O dissociation step is required to generate intermediate H;64 then the reactions are:

Volmer step: \* + 
$$H_2O + e^- \rightarrow *H + OH^-$$
 (4)

Heyrovsky step: \*H + 
$$H_2O$$
 +  $e^- \rightarrow *H_2 + OH^-$  (5)

Tafel step: 
$$*H + *H \rightarrow *H_2$$
 (6)

Previous studies showed that the activity of HER electrocatalysts is closely related to the thermodynamic adsorption of intermediate H on the surface of electrocatalysts, whose strength can be evaluated by the Gibbs free energy of H adsorption  $(\Delta G_{\rm H}^*)^{.36}$  The widely accepted equation for calculating the  $\Delta G_{\rm H}^*$  is:<sup>36,49</sup>

$$\Delta G_{\rm H}^* = \Delta E_{\rm H}^* - T\Delta S + \Delta Z PE + \Delta E_{\rm solvation} \tag{7}$$

where  $\Delta E_{\rm H}^*$  is the enthalpy difference between the surface with and without hydrogen,  $T\Delta S$  is the entropy contribution, and  $\Delta ZPE$ is the change of zero-point energy while  $\Delta E_{\rm solvation}$  is the change of the solvation energy contribution. There are different methods to calculate solvation energy. Each method has its own pros and cons, which will be discussed in section 4.3.2.2. If  $\Delta G_{\rm H}^*$  is much smaller than 0, it means that the adsorption of H on the surface is too strong, which makes it is hard for H to desorb from the surface and would lead to a high energy barrier for the Heyrovsky/Tafel step. On the other hand, a very positive  $\Delta \textit{G}_{H}^{*}$  would cause a high energy barrier for the Volmer step. A value of  $\Delta G_{\rm H}^*$  close to 0 represents the optimal thermodynamic adsorption for hydrogen. This relationship proposed by Nørskov et al. is called the "Volcano plot".65 The yaxis of the "Volcano plot" represents the exchange current density  $(j_0)$ , an experimental parameter to evaluate the intrinsic activity of the electrocatalyst. The larger the  $j_0$ , the higher the intrinsic activity. While tuning the value of  $\Delta G_{\rm H}^*$  has been proved to be an effective approach to enhance the activity of some HER catalysts, it is necessary to point out that a  $\Delta G_{\rm H}^*$  close to 0 does not guarantee a high HER activity, which depends on other parameters as well.36 Some commonly used approaches for tuning the value of  $\Delta G_{\rm H}^*$  of HER electrocatalysts are discussed in the following part.

2.1.1. Heteroatom doping. Doping is one of the most widely used approaches to tune the physical and chemical properties of pristine materials and found to be effective in manipulating  $\Delta G_{H}^{*}$  via redistributing charge, creating dangling bonds, changing the coordination numbers, etc. 20,66 For examples, NiCo<sub>2</sub>S<sub>4</sub> is an active HER electrocatalyst because of its high conductivity and the presence of hybrid d orbitals between Ni and Co.58 However, its activity was hindered by the strong interaction between H and S sites, which slows down the kinetics of H desorption from these sites. 67,68 Wu et al. successfully modulated the electron density of NiCo2S4 and facilitated the desorption of H from those S sites via the incorporation of N dopants.58 Due to the strong electronegativity of N, the electron density of S decreases after N doping, which makes the desorption of H from these S sites easier. The concept of N doping was also tested for other metal sulfides, including FeS2, NiS2, and CoS2. All of them showed an obvious performance improvement, suggesting that it is a general approach to tune the electron density of S sites in metal sulfides. Ni<sub>3</sub>S<sub>2</sub> is also a promising HER electrocatalyst because of its metallic properties that can facilitate interfacial charge transfer. However, the adsorption of H on S sites is also not favorable and limits the performance of Ni<sub>3</sub>S<sub>2</sub>. Recently, Kou et al. demonstrated that the incorporation of N into Ni<sub>3</sub>S<sub>2</sub> can address this issue.<sup>69</sup> DFT calculation found that the coordination number of S decreased after N doping and more dangling bonds were exposed, which facilitated the adsorption of H. In addition, the incorporated N dopants can serve as new active H adsorption sites, depending on the coordination number of N. If the coordination number of N is low (e.g., 3), then too many exposed dangling bonds coupled with the strong electronegativity of N make the adsorption of H on N sites too strong. In contrast, if the coordination number of N is high (e.g., 5), the fewer dangling bonds combined with the strong electronegativity of N create a favorable  $\Delta G_H^*$  on N sites. The role of N is to tune the coordination number of S and serve as a potential active H adsorption site. NiO is another well studied HER electrocatalyst since it is favorable for the adsorption and dissociation of H<sub>2</sub>O molecules. However, the overall performance of pristine NiO is limited by its unfavorable H adsorption activity. Kou et al. tackled this issue by doping carbon into NiO to switch the H adsorption activity of NiO.60 The carbon doped NiO achieved an ultralow overpotential of 27 mV at a current density of 10 mA cm<sup>-2</sup>. DFT calculation found that the carbon dopant distorted the local structure of NiO and decreased the coordination number of outermost layer Ni sites from 3 to 2, which enriched the electron density on these Ni sites as evidenced by the consistent agreement between the projected density of states (PDOS), electron density mapping and atomic charge difference ( $\Delta Q$ ) analysis, as shown in Fig. 3. The analysis further revealed that the shift of  $\Delta G_{\rm H}^*$  is associated with two factors, the number of Ni sites that H bind to and the  $\Delta Q$  of Ni. If the structure has similar  $\Delta Q$ , then the more Ni sites that H bind to give a  $\Delta G_{\rm H}^*$  closer to 0, which is due to the stronger interaction between H and multi-fold Ni. On the other hand, if H binds to the same number of Ni sites, then a larger  $\Delta Q$  gives

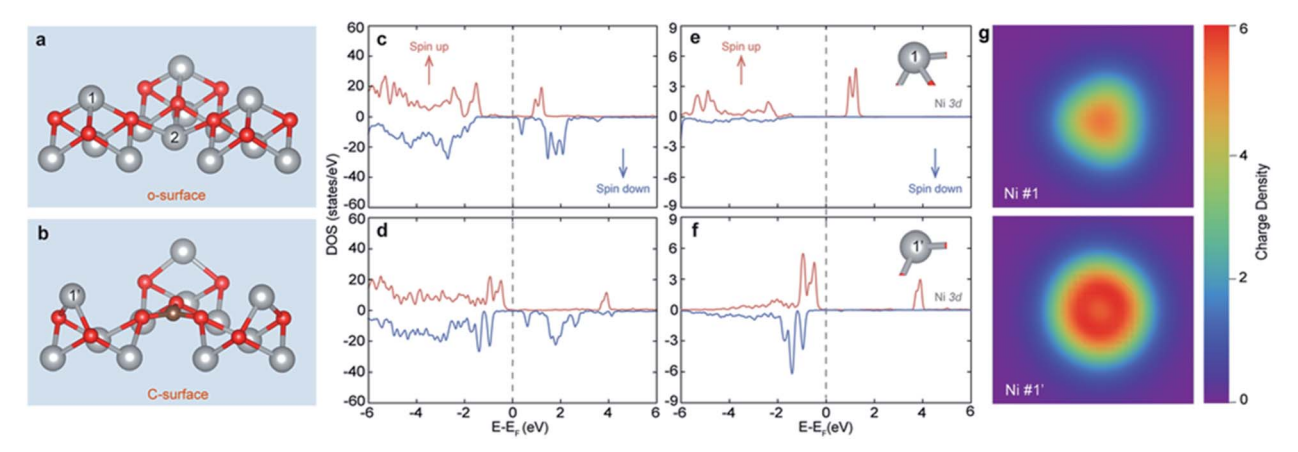


Fig. 3 Surface structure, PDOS and electron density mapping of the o-surface and C-surface. (a) and (b) the structures of the o-surface and C-surface. (c) and (d) the PDOS of the Ni 3d and O 2p of the first three layers from the o-surface and C-surface. (e) and (f) the PDOS of the 3d orbitals of Ni on the o-surface (Ni #1) and C-surface (Ni #1'), respectively. (g) Charge density mapping of the outermost Ni (#1 and 1') on the o-surface (upper) and C-surface (bottom). Reprinted from ref. 60, copyright 2020, with permission from Springer.

a  $\Delta G_H^*$  closer to 0, because the higher electron density of Ni makes it easier for H to bind with it. It is anticipated that other n-type dopants such as Si, N and P with a smaller atomic size than Ni could have a similar effect to the carbon dopant in tuning the electron density of Ni sites and H adsorption activity on them.

2.1.2. Vacancy engineering. The thermodynamic adsorption of H strongly depends on the coordination number of active sites. The existence of vacancies on the catalyst surface can create under-coordinated sites, which have more dangling bonds and usually show higher activity than the regular fully coordinated sites.21 Therefore, vacancy engineering is another effective approach to adjust the thermodynamic adsorption of H. For example, in an early study, Raybaud et al. reported that the basal plane of 2H phase MoS2 is inactive toward the adsorption of H.70 How to activate the basal plane of 2H phase MoS<sub>2</sub> has been a challenging and interesting topic in the field. Li et al. successfully demonstrated how to activate the basal plane of 2H phase MoS<sub>2</sub> through the synergistic effect of strain and S vacancies.41 The capillary force was first introduced to strain the lattice of MoS2, followed by Ar plasma etching to create S vacancies on the surface. The level of strain and the concentration of S vacancies were controlled by adjusting the topography of the gold nanocones and the Ar plasma etching time. DFT calculation showed that the introduction of S vacancies on the surface brings about more gap states near the Fermi level, allowing H to adsorb on the exposed Mo sites easily. On the other hand, the applied tensile strain shifted both the valence band maximum (VBM) and conduction band minimum (CBM) closer to the Fermi level, resulting in a narrower bandgap and more gap states, which also facilitated the adsorption of H. The strain and vacancy engineered basal plane of 2H-MoS<sub>2</sub> showed an even higher activity than the edge-site only MoS<sub>2</sub>. Tungsten trioxide (WO<sub>3</sub>) is another attractive material for the HER because of its high abundance and excellent electrochemical stability for the HER. However, its activity is hampered by its poor conductivity and unfavorable H adsorption activity.

In order to solve these issues, Zheng *et al.* introduced oxygen vacancies into the structure of  $WO_3$  by the liquid exfoliation method. The concentration of oxygen vacancies was controlled by the annealing time in air. The authors demonstrated that the enriched oxygen vacancies in the structure introduced more gap states, which simultaneously improves the conductivity and the H adsorption activity of  $WO_{3-x}$ .

2.1.3. Strain engineering. Strain engineering is another commonly used method to manipulate the H adsorption activity of catalysts via tuning the DOS of active sites near the Fermi level.<sup>22,72,73</sup> For example, Voiry et al. systematically studied the role of strain in tuning the  $\Delta G_{\rm H}^*$  of WS<sub>2</sub>.<sup>74</sup> By chemically exfoliating lithium intercalated WS2 powder, strain was introduced into the exfoliated monolayer WS2 nanosheet (NS) and observed by using a high-angle annular dark-field (HAADF) aberration-corrected scanning transmission electron microscope (STEM). The authors performed DFT calculation and found that by gradually increasing strain from 0 to 4% on metallic 1T phase WS2, the DOS near the Fermi level increased accordingly. As a result, the value of  $\Delta G_{H}^{*}$  shifted from 0.28 eV to -0.15 eV. Interestingly, the HER activity was not improved when the strain was applied on semiconducting 2H phase WS<sub>2</sub>. They also found that only tensile strain can tune  $\Delta G_{H}^{*}$  effectively while compressive strain did not. The combination of experiments and DFT proved that the tensile strain must couple with a 1T metallic phase to facilitate the adsorption of H on WS<sub>2</sub>.

d Band theory can be used to well explain how strain tunes the value of  $\Delta G_{\rm H}^*$  for metal systems. The principle of d band theory is that the adsorption strength of adsorbates on a surface strongly depends on its surface electronic structure. For example, when oxygen-containing species are adsorbed on a metal, the p orbitals of oxygen interact with the d orbitals of the metal to generate bonding orbitals and antibonding orbitals. The formation of bonding orbitals is similar for all metal surfaces. However, the filling of antibonding orbitals is strongly affected by the d band level of the metal surface. A deeper d-band center would lead to an increased filling of

antibonding orbitals and weaken the bonding of adsorbates. The d band center could be manipulated by the introduction of strain. Yan et al. systematically studied the effect of strain on different metals (e.g., Ni, Cu, and Pt) towards the HER.78 Since these metals lie in different positions in the "Volcano plot", they have different responses to the strain. For example, the positions of Ni and Pt on the left side of the volcano plot indicate a very strong H adsorption. The application of compressive strain shifts the d band center down. A deeper d band means a larger overlap with the orbitals of H and more antibonding orbitals are filled, which destabilizes the adsorption of H and makes  $\Delta G_{\rm H}^*$  closer to 0. In contrast, the H adsorption on Cu is weak, so tensile strain should be applied to upshift the d band center and consequently stabilize the adsorption of H. Their experimental results are consistent with the DFT calculation results and the d band theory, demonstrating that strain engineering can serve as an effective approach to tune the activity of H adsorption. 75,76,78-80 Li et al. demonstrated a good example of how to combine strain engineering with other strategies to steer the adsorption/desorption of intermediates.81 Ag has been considered to be an inactive HER electrocatalyst for decades. One of the reasons is the weak adsorption of H on the surface of Ag. Li et al. successfully tackled this issue through the laser ablation in liquid method to introduce a high density of stacking faults, which created a low coordination number environment and high tensile strain in the structure. DFT calculation found that the coupling of a low coordination number and tensile strain together successfully manipulated the adsorption activity of H on the surface of Ag. The  $\Delta G_{\rm H}^*$  of the Ag (111) surface shifted from ~0.6 eV to the optimal thermodynamic value of 0 on a strained Ag surface (Fig. 4c and d). Wang et al. also used strain engineering to tune the activity of two-dimensional

transition metals for the HER.82 Interestingly, they didn't use any heterogeneous substrate to generate strain; instead, intrinsic strain was introduced and fine-tuned by controlling the thickness of two-dimensional transition metal nanosheets since the cleavage of bulk metal atoms often leads to charge redistribution and attractive interactions between surface atoms. The DFT calculation revealed that the attractive interaction between surface atoms introduces surface tensile strain, and the level of strain is inversely proportional to the thickness of nanosheets. Likewise, the HER activity of Pd nanosheets was also experimentally found to be strongly correlated with the thickness of Pd nanosheets, again proving the success of strain engineering in tuning the HER performance of metals.

### 2.2. Kinetics of H<sub>2</sub>O dissociation

It's well known that the activity of Pt in alkaline medium is two to three orders lower than that in acidic media.83 There are different explanations.32,84-89 Although some of them are still controversial, one of the most widely accepted explanations attributes this phenomenon to the pH dependence of the energy barrier for the dissociation of H2O molecules in alkaline medium.90 Therefore, it is important to consider this factor in evaluating or designing new HER electrocatalysts. According to the Arrhenius equation, the energy barrier can be determined by plotting the reaction rate as a function of temperature.<sup>91</sup> It's highly recommended to use the stable current extracted from current-time measurements with a dwell time of at least 5 minutes and then use the following equation to convert current density (j) to reaction rates (R): $^{49}$ 

$$\log_{10} j(\eta) = \log_{10} (nFN_{A}^{-1}R(\eta))$$
 (8)

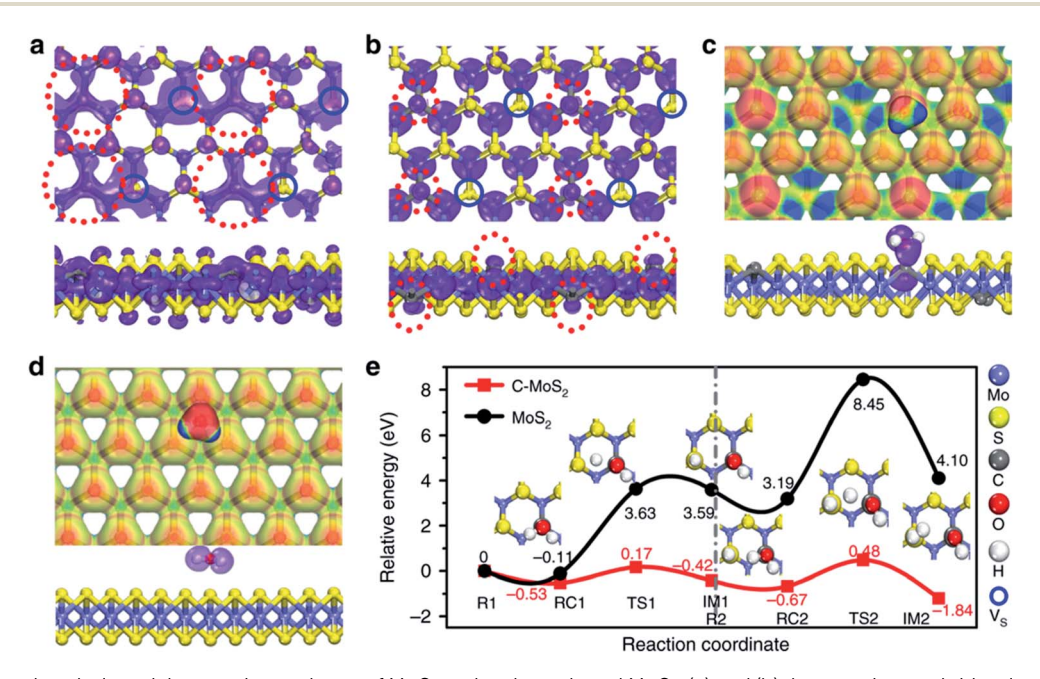


Fig. 4 The structural analysis and the reaction pathway of MoS<sub>2</sub> and carbon-doped MoS<sub>2</sub>. (a) and (b) the top-view and side-view of the sp<sup>2</sup> hybrid orbitals (highlighted by the dashed red circle) of (a) MoS<sub>2</sub> and (b) carbon-doped MoS<sub>2</sub>. (c) and (d) The top-view and side-view electrostatic potential of adsorbed H<sub>2</sub>O on the surface of (c) carbon-doped MoS<sub>2</sub> and (d) MoS<sub>2</sub>. (e) The reaction pathway of the HER on the surface of MoS<sub>2</sub> and carbon-doped MoS<sub>2</sub>. Reprinted from ref. 23, copyright 2019, with permission from Springer.

It is noteworthy that the energy barrier extracted from this method includes not only the combined energy barriers of the elementary steps (Volmer step and Heyrovsky/Tafel step) of the HER but also the barriers originated from the mass diffusion of bubbles and reactants. As a result, sometimes it's hard to compare the experimental data with the calculated data, which does not consider the factor of mass transfer. There are two general methods to calculate the energy barrier of H<sub>2</sub>O dissociation, ab initio molecular dynamics (MD) free energy sampling and static configuration. For the former, one can evaluate the forces using quantum mechanics (e.g., DFT) and move atoms based on classical Newton's equation (often termed ab initio MD). To get the reaction barriers, one needs to use enhanced sampling methods such as meta-dynamics and constrained MD at finite temperature for the catalyst systems with explicit liquid water. Such methods are expensive and have been applied only to limited systems. 50,51 The latter is a cheaper and more commonly used method, but it requires careful examination of water interaction with the catalyst surface. In this review, we mainly focus on static configuration calculation, and the two most commonly used DFT calculation methods will be reviewed here. The first one is the Nudged Elastic Band (NEB) method, which aims to determine the saddle point and find the minimum reaction pathway between the known reactants and products. 92,93 A series of intermediates along the reaction pathway will be generated through the linear combination of the initial structure and final structure, and every image would be optimized to find the lowest possible energy, which is constrained by a spring force between different images and projecting out the component of the force. Different from the NEB method, which is an interpolation method to find the reaction pathway and transition state, the DIMER method, a local saddle-point search algorithm method via computing either exact or approximate Hessians, can also be used to search for the transition state. DIMER calculation starts from a minimum basin and searches in random directions until it finds the SP. This method is aimed to deal with systems with a complicated reaction pathway in high dimensional configuration space. Due to the slow convergence of NEB calculation, the DIMER method can be coupled with the NEB method to speed up the calculation and help find the saddle point accurately.94

Given the important role of the H<sub>2</sub>O dissociation step for the HER, several approaches have been reported to improve the kinetics of H<sub>2</sub>O dissociation. Two commonly used approaches are discussed in the following part.

**2.2.1. Orbital engineering.** The dissociation of H<sub>2</sub>O molecules on the surface of HER electrocatalysts largely depends on the orbital orientation of active sites. An unfavorable orbital orientation could slow down the kinetics of H<sub>2</sub>O dissociation.<sup>23</sup> For example, MoS<sub>2</sub> typically shows a decent HER performance in an acidic medium because of the favorable adsorption of protons.<sup>36</sup> However, its performance is much lower in an alkaline medium because its orbital orientation is not favorable for the adsorption and dissociation of H<sub>2</sub>O molecules.<sup>95</sup> Recently Zang *et al.* have successfully solved this problem by doping MoS<sub>2</sub> with carbon.<sup>23</sup> The carbon doped MoS<sub>2</sub> achieved a current density of 10 mA cm<sup>-2</sup> with an overpotential of only 45 mV,

which is the best performance among all ever reported MoS<sub>2</sub> based materials in alkaline medium. Their DFT calculation found that the carbon dopant formed an sp2 hybridization structure in MoS2 and created an empty 2p orbital. The vertical characteristic of the empty 2p orbital facilitates the adsorption and dissociation of H<sub>2</sub>O molecules (Fig. 4). Their DFT calculation and experimental results consistently proved the role of carbon in manipulating the orbital orientation to facilitate H<sub>2</sub>O dissociation. It is anticipated that the lower HER activity of Pt in alkaline medium is also due to the slow kinetics of H2O dissociation, as a result of the unfavorable orbital orientation. Xie et al. demonstrated how to tune the orbital orientation of Pt-Ni nanowires via N doping, which specifically bonded with Ni sites and provided an empty dz2 orbital.96 The surface electrostatic potential mapping analysis revealed the importance of empty dz2 orbitals for the adsorption and dissociation of H2O molecules. The N doping method was also employed to tackle the unfavorable orbital orientation in Pt-Co and Pt-Cu structures. All these N doped Pt-based alloys showed enhanced HER performance. These previous studies prove that orbital engineering is an effective approach to facilitate the dissociation of H<sub>2</sub>O molecules in an alkaline medium.

2.2.2. Constructing a heterogeneous interface. Metal oxides/hydroxides are highly favorable for H2O dissociation.97,98 An effective strategy to promote the kinetics of H<sub>2</sub>O dissociation is to integrate them with metal-based HER electrocatalysts. For example, Subbaraman et al. deposited nanoscale Ni(OH)2 clusters on the Pt surface and observed activity enhancement by a factor of 8 for the HER in alkaline medium, compared to the control sample without metal hydroxide clusters.24 They attributed the enhancement to the synergistic effect between Ni(OH)2 and Pt, and the proposed schematic is depicted in Fig. 5a. The H<sub>2</sub>O was dissociated on the edges of Ni(OH)<sub>2</sub> clusters first, and then the generated H migrated to nearby Pt and recombined with each other to form an H2 molecule. By introducing Li+ ions into the compact portion of the double layered hydroxide, the noncovalent interaction (van der Waals interaction) between hydrated cations (AC<sup>+</sup>) and adsorbed OH<sup>-</sup> leads to the formation of OH<sub>ad</sub>-AC<sup>+</sup>(H<sub>2</sub>O)<sub>x</sub> complexes, which can induce the destabilization of the H-OH bond and further improve the activity (Fig. 5c). This is one of the pioneering studies on utilizing water dissociation promoters such as Ni(OH)2, to accelerate the kinetics of H2O dissociation and, thus, enhance the HER activity. Although the authors didn't include theoretical calculation in this work, the proposed mechanism was widely accepted by the scientific community and verified by other groups later.99-101 This strategy was also extended to other catalytic systems. Niu et al. reported a Ni<sub>3</sub>N/ MoO<sub>2</sub> heterogeneous structure, in which the two materials worked synergistically.20 DFT calculation revealed that the unoccupied orbital center of MoO2 is low, which facilitated the H<sub>2</sub>O dissociation, while Ni<sub>3</sub>N possesses a favorable H adsorption activity, with a  $\Delta G_{\rm H}^*$  of -0.08 eV. Therefore, the MoO<sub>2</sub>/NiN<sub>3</sub> heterostructure required only an ultra-small overpotential of 21 mV to achieve a current density of 10 mA cm $^{-2}$ , which is one of the best HER performances. A similar synergistic effect was reported for other systems. Dinh et al. also reported a metal/ metal oxide heterogeneous HER electrocatalyst, which showed strong adsorption toward intermediate H and OH-, respectively, and led to the destabilization of H<sub>2</sub>O molecules.<sup>102</sup> The authors tested a series combination of metals and metal oxides and finally identified Ni and CrO<sub>r</sub> as the suitable metal and metal oxide. Ni and CrO<sub>x</sub> were co-deposited on a Cu substrate (denoted as CrOx/Ni-Cu), which achieved an overpotential of 48 mV at a current density of 10 mA cm<sup>-2</sup>, one of the best reported HER performances in neutral medium. To verify the destabilization effect induced by the co-existence of Ni and CrO<sub>x</sub>, the authors calculated the energy barrier of H<sub>2</sub>O dissociation on different surfaces (Cu, Cu-Ni, CrOx/Cu and CrOx/Ni-Cu) and found that the energy barrier on CrO<sub>x</sub>/Ni-Cu has the smallest value of 0.64 eV.

### 2.3. Thermodynamic adsorption of OH

According to the Brønsted-Evans-Polanyi (BEP) relationship, the energy barrier of a chemical reaction depends on the enthalpy difference between the initial state and the final state. 103-105 When the energy of the final state is lower than that of the initial state, the energy barrier is typically lower. This rule also applies to the process of H<sub>2</sub>O dissociation. Since the energy barrier of H<sub>2</sub>O dissociation relies on the final state energy, it would be affected by the adsorption of intermediate H and OH<sup>-</sup>. The thermodynamics of the adsorption of intermediate H on the catalyst surface has been extensively studied and a consensus has been reached in the community that an optimal value of  $\Delta G_{\rm H}^*$  should be close to 0. Yet, the role of OH<sup>-</sup> adsorption has been rarely studied, although it can also significantly affect the HER activity. If the adsorption of OH on the surface is too strong, while the energy barrier of H2O dissociation would be lower it could take too much energy to remove the adsorbed OH<sup>-</sup> from the surface, which poisons the active sites and slows down the kinetics of the HER. In contrast, if the adsorption is too weak, then the energy barrier of H<sub>2</sub>O dissociation would be high and the kinetics of H<sub>2</sub>O dissociation would limit the HER performance.25 Therefore, the adsorption of OH<sup>-</sup> should also be optimized. Subbaraman et al. investigated the HER activity on 3d M(Ni, Co, Fe, and Mn) hydro(oxy) oxide surfaces and found that it decreases with the strength of the M-OH bond (Ni, Co, Fe, and Mn).84 This relationship is independent of the source of OH-, no matter whether the OHis from the electrolyte or the product of H<sub>2</sub>O dissociation. Their

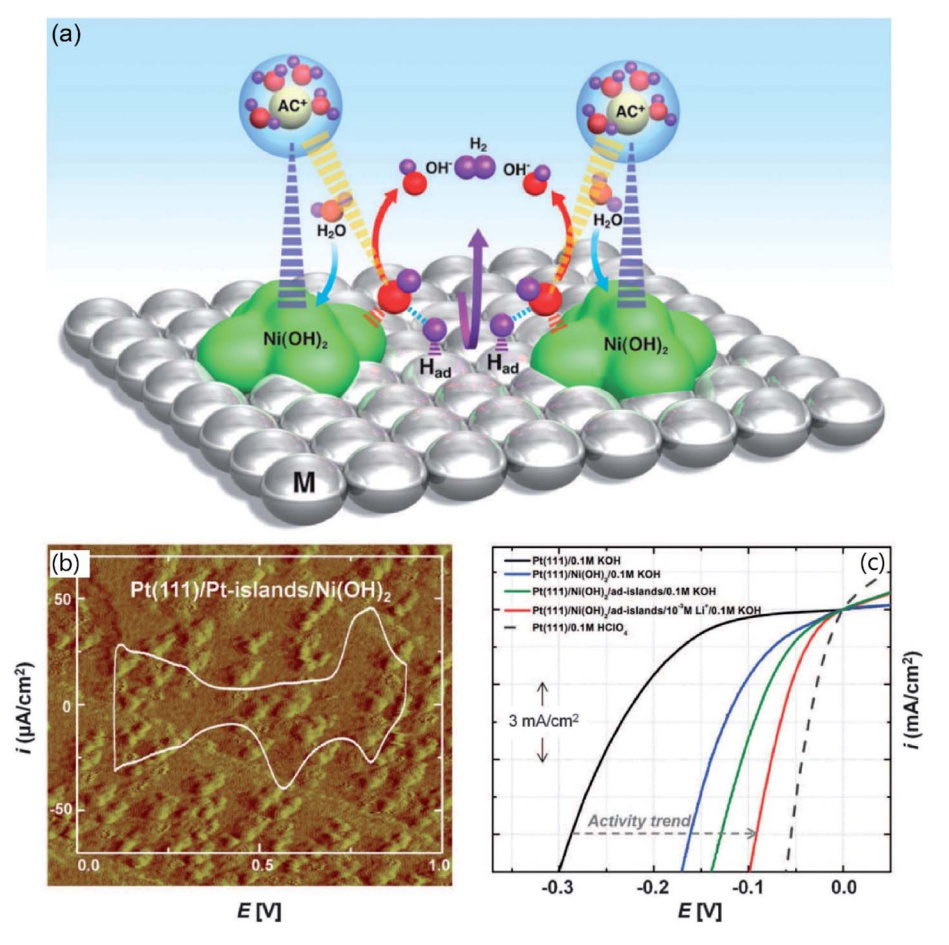


Fig. 5 Coupling of Ni(OH)<sub>2</sub> with Pt for an efficient HER in alkaline medium. (a) The schematic diagram of the working mechanism of the Ni(OH)<sub>2</sub>/ Pt heterostructure; (b) the STEM image and cyclic voltammetry (CV) curve of the Ni(OH)<sub>2</sub>/Pt-islands/Pt(111) surface; (c) the HER activity comparison of a series of Pt surfaces modified with different surface structures. Reprinted from ref. 24, copyright 2011, with permission from the American Association for the Advancement of Science

work provided a possible strategy to tune the adsorption of OH<sup>-</sup> by changing the bond strength of M-OH. The authors also investigated the effect of optimizing the adsorption of OH<sup>-</sup> on the surface for the hydrogen oxidation reaction (HOR). By introducing more defects on the surface of Ir, the adsorption of OH<sup>-</sup> on the surface was facilitated and consequently, the HOR activity was boosted.<sup>85</sup> They also found that the PtRu alloy has a higher activity than Pt because of the existence of Ru that facilitates the adsorption of OH<sup>-</sup>. The findings on the OH<sup>-</sup> adsorption in the HOR provide important insights into the HER.

### 2.4. Conductivity

The electrode conductivity of the electrode is determined by three factors: (1) the conductivity of the catalyst, (2) the conductivity of the substrate (or the current collector), and (3) the electric contact between the catalyst and substrate. The improvement of any of these three factors could improve the electrode conductivity and, thus, enhance HER activity. A representative example is  $MoS_2$ , which has two common phases, semiconducting 2H phase and metallic 1T phase.<sup>26</sup> Lukowski *et al.* reported an exfoliation method to prepare 1T phase  $MoS_2$ , which achieved a current density of 10 mA cm<sup>-2</sup>

with an overpotential of 187 mV.40 This value is much better than that of 2H phase MoS<sub>2</sub> (Fig. 6a). The enhanced performance was attributed to the better conductivity of the electrocatalyst. Alternatively, if the active catalyst material is less conductive, it is typically deposited on a current collector. There are numerous reports on how to grow catalysts on conducting substrates such as graphene,106 carbon nanotubes,107 Ni foam,108 etc. For example, Li et al. grew MoS<sub>2</sub> on reduced graphene oxide (RGO) and achieved a small Tafel slope of 41 mV  $dec^{-1}$ , which is much smaller than that of MoS2 nanoparticles without the substrate (Fig. 6b).106 Nevertheless, these three factors are often coupled with each other and it's hard to distinguish the contribution of each factor to the electrode conductivity. For example, the improvement of the conductivity of the catalyst or substrate would also reduce the contact resistance between them. Voiry et al. studied the effect of contact resistance  $(R_c)$ between the substrate and MoS2 for HER activity. 109 By carefully controlling the treatment of 2H phase MoS2 with n-butyllithium, 2H phase MoS2 was converted to 1T phase MoS2 to different extents and consequently, the  $R_c$  was reduced. As a result, the efficiency of electron injection from the electrode to the catalyst was improved. The phase engineered MoS<sub>2</sub> achieved an onset potential of  $\sim -0.1$  V and a Tafel step of  $\sim 50$  mV dec<sup>-1</sup>,

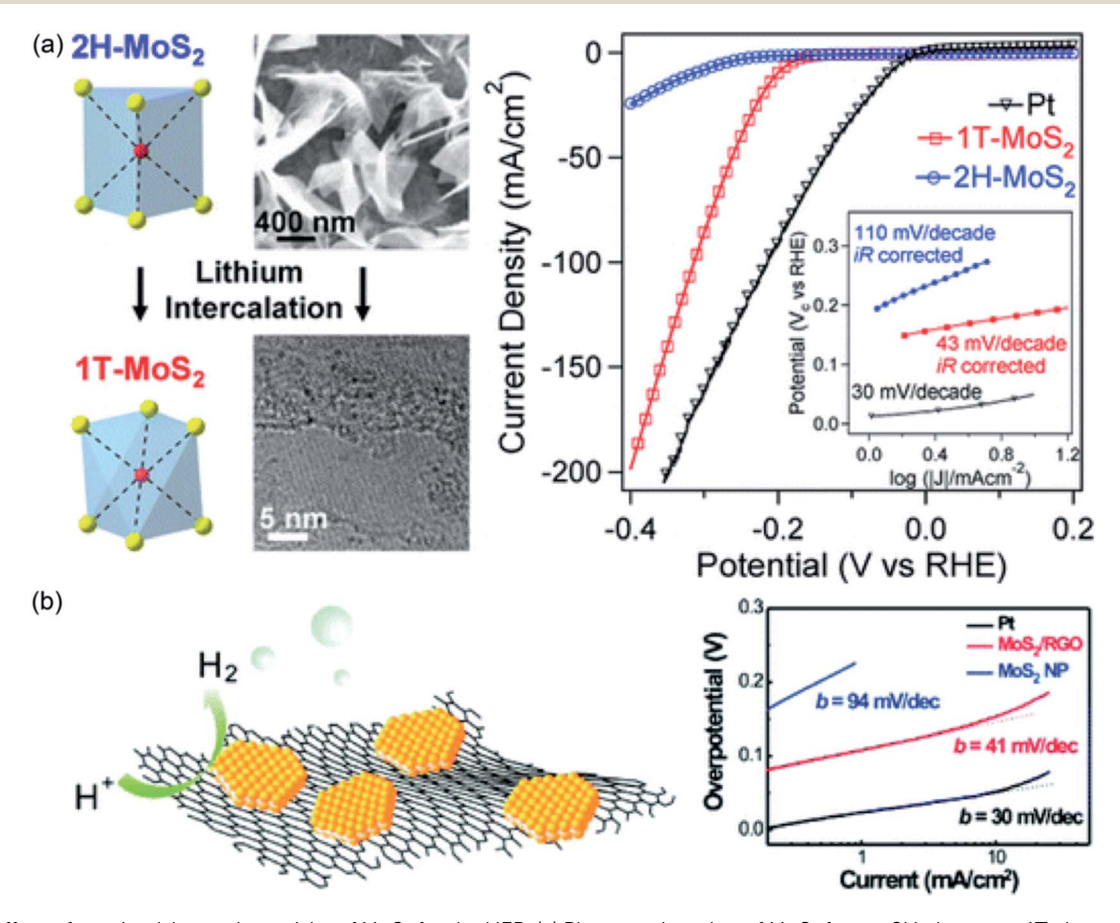


Fig. 6 The effect of conductivity on the activity of  $MoS_2$  for the HER. (a) Phase engineering of  $MoS_2$  from a 2H phase to a 1T phase to improve its conductivity; (b) coupling  $MoS_2$  with graphene to improve the conductivity of the substrate and electric contact. (a) Reprinted from ref. 40, copyright 2013, with permission from American Chemistry Society; (b) reprinted from ref. 106, copyright 2011, with permission from American Chemistry Society.

comparable to those of 1T phase MoS2. The authors claimed that the basal plane of 2H MoS<sub>2</sub> with S vacancies is active toward the HER, but it is rendered inactive because of the high  $R_c$ between the MoS2 and the substrate. This problem was alleviated by minimizing the  $R_c$ . In addition to directly deposit the catalyst material onto a current collector, avoiding using nonconductive binders such as Nafion is also important for reducing the R<sub>c</sub> between the substrate and the catalyst. 110

### 2.5. Charge transfer

Charge transfer between the catalyst surface and electrolyte is another important factor governing the HER activity of an electrocatalyst. It can be evaluated from the charge transfer resistance (Rct) extracted from Nyquist plots by performing electrochemical impedance spectroscopy (EIS).27 If the Nyquist plot has a semi-circle, the diameter of the circle can be approximated as the  $R_{ct}$  value of the system. The larger the diameter, the larger the  $R_{\rm ct}$ .  $R_{\rm ct}$  is determined by many factors such as the applied potential on the working electrode, the conductivity of the catalyst, the contact surface area between the catalyst and electrolyte, the conductivity of the electrolyte, etc. The improvement of any of these factors would decrease the  $R_{ct}$ . For example, the larger the applied potential, the larger the driving force for the transfer of electrons. When the electrode materials have better conductivity, the  $R_{ct}$  is also smaller. Increasing the contact surface area between the catalyst and electrolyte would also decrease the Rct, because contact resistance is inversely proportional to the surface area of electron transport. Finally, improving the conductivity of the electrolyte, by increasing the concentration of conductive species or using more conductive species in the electrolyte, is also helpful. For example, Patil et al. showed that when increasing the concentration of the KCl electrolyte from 10 mM to 100 mM and final 500 mM, the HER activity of the catalyst increased accordingly.111

#### 2.6. Bubble effect

When bubbles are generated on the surface of catalysts, they don't detach from the electrode surface immediately. Instead, they attach on the surface of the electrode and grow to a certain size before they leave the surface in the form of bubbles. The covered bubbles will hamper the electron transfer between the catalyst and electrolyte, which increases the electric resistance and causes a voltage drop. This effect is called the bubble effect.64,112,113 The bubble effect mainly includes two parts: the surface area reduction by bubble coverage and the formation of a bubble froth layer. Usually, the higher the current density, the higher the bubble coverage on the catalyst surface. Qian et al. reported that the ohmic resistance is proportional to the bubble coverage.114 One of the commonly used approaches to mitigate the bubble effect is to create nanostructures, which make it easier for bubbles to release from the electrode surface. Lu et al. synthesized a nanostructured MoS2 film, which showed a much higher activity toward the HER compared to the flat film.<sup>28</sup> Adhesive force measurements found that the adhesive force of bubbles on a nanostructured surface is much smaller than that on the flat surface, as indicated by the smaller bubble size on nanostructured MoS<sub>2</sub> (Fig. 7). The second approach to minimize the bubble effect is to make the electrode surface superaerophobic. For example, Hao et al. synthesized Cu<sub>3</sub>P

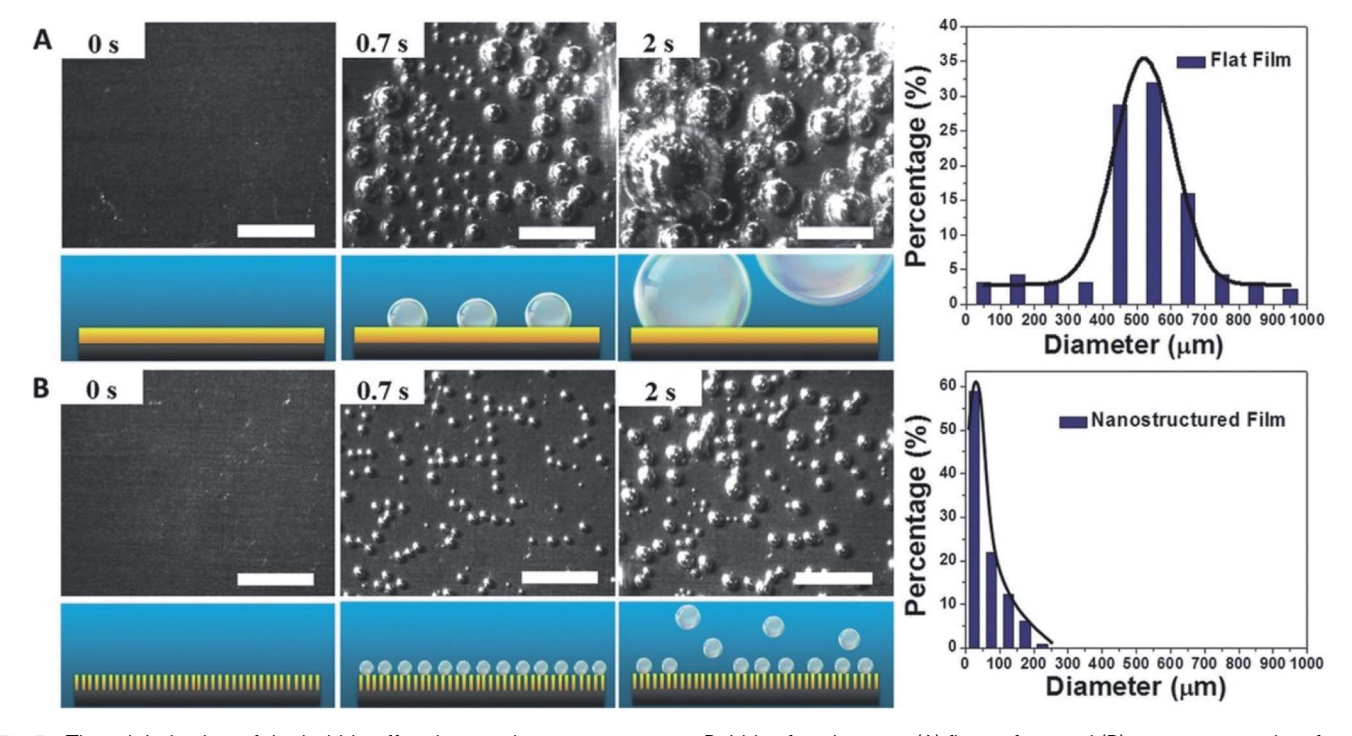


Fig. 7 The minimization of the bubble effect by creating nanostructures. Bubbles forming on a (A) flat surface and (B) nanostructured surface. Reprinted from ref. 28, copyright 2014, with permission from Wiley-VCH.

microsheets and they showed a high activity toward catalyzing the HER and OER.<sup>29</sup> The authors measured the contact angle of bubbles on the surface of materials and found that the contact angle on the superaerophobic surface was larger than those of control samples, suggesting that the superaerophobic surface facilitates the detachment of bubbles. However, it is noteworthy that the superaerophobic characteristic also makes it harder for electrolytes to get access to the active sites on the catalyst surface. Therefore, a balance has to be maintained if this strategy is employed.

### 2.7. Stability

The stability of electrocatalysts is of great importance for practical applications and it has rarely been studied seriously. There are two ways to experimentally characterize the stability of electrocatalysts.61 The first one is the current-time test. A constant potential is applied and how the current changes with time is recorded. This method is closer to the practical application. The second method is CV cycling, which is also called the accelerated stability test. Using this method, the electrodes are scanned in the HER potential window for a certain number of cycles, and the LSV curves before and after CV cycling are compared with each other. The better the overlap of LSV curves before and after CV cycling, the better the stability. It's worth mentioning that both methods are qualitative measurements. Recently, Geiger et al. proposed a metric-stability number to evaluate the stability of electrocatalysts quantitatively. 115 The definition of the stability number is the ratio of the amount of evolved gas to the amount of dissolved catalyst. The larger the number, the better the stability. They used this method to study the IrO2 system for the OER and made a quantitative comparison between different samples. However, the application of the stability number is limited in certain situations. For example, if the catalyst degradation mechanism is particle aggregation, which doesn't involve particle dissolution, then it's hard to use the stability number to evaluate the stability of the catalyst. Theoretically, the stability of an electrocatalyst could be simulated by calculating the Pourbaix diagram of the material. In this way, the thermodynamically stable phase under working conditions can be found, but this method cannot take the kinetics of material evolution into consideration. If the electrocatalyst is transforming from its semi-stable phase to a thermodynamically stable phase under the working conditions and the process is very slow, then the Pourbaix diagram cannot capture this process and will only give the thermodynamically stable phase, which could be misleading. Another way to simulate the stability of the catalyst is to perform MD simulation, which however is only able to evaluate the catalyst's stability on a very short-time scale and cannot reflect the activity variation over a long time scale.116

There are several mechanisms for the degradation of electrocatalysts, including particle detachment, dissolution, aggregation, and carbon corrosion.<sup>31</sup> One important technique that has been used to probe the degradation mechanism of catalysts is identical location transmission electron microscopy (ILTEM).<sup>117,118</sup> The same position before and after

measurements will be located and compared to reveal the change of the catalyst during the tests. For example, Mayrhofe et al. found that the absolute number of Pt/C particles decreased a lot after electrochemical tests, while there was only a very small increase of particle size, indicating that a lot of the particles detached from the surface in the electrochemical tests.117,118 The dissolution of Pt can also be observed under ILTEM. Although Pt is very stable, it can still dissolve at pH < 2 and potential beyond 0.85 V vs. the standard hydrogen electrode (SHE), according to the Pourbaix diagram of Pt (25 °C). 119 Perez-Alonso et al. observed the dissolution of Pt by using ILTEM. 120 They observed that both the number and the size of Pt particles decreased after 3000 degradation cycles between 0.6 V and 1.2 V versus the reversible hydrogen electrode (RHE), suggesting the detachment and dissolution of Pt particles. Particle aggregation is another mechanism of catalyst degradation. 30,121-123 The aggregation of particles is often due to the migration of particles, which can be directly observed under ILTEM. As shown in Fig. 8a and b, separate Pt particles aggregate into "string-shape" clusters after electrochemical measurements, indicating that the migration caused the aggregation of Pt particles. Similar "string-shape", "L-shape" or "T-shape" clusters were observed in other areas under ILTEM. Carbon corrosion is another degradation mechanism. 121,124,125 It has been commonly observed in fuel cells since their relatively high operation temperature can speed up the corrosion of the carbon support. As a result, the porosity decreases and limits the mass transfer. It is important to point out that multiple degradation processes often occur at the same time during catalytic reactions (Fig. 8c and d).

Long-term stability is a very important aspect of any electrocatalyst and extending the lifetime of the catalyst is always desired. Some general approaches have been demonstrated to be useful in enhancing the long-term stability of HER catalysts. First, binder-free electrocatalysts are preferred over powdered form catalysts because electrolysis is performed at high currents in practical systems, and powders are more likely to disintegrate from the electrode under these conditions. Second, the active phase of HER materials should be a thermodynamically stable phase, because the meta-stable phase has the risk of being reduced back to the thermodynamically stable phase during the HER. For example, if Ag<sub>2</sub>O is used as a HER electrocatalyst, it will be reduced to form metallic Ag during the reaction according to the Pourbaix diagram and lose its activity. 126 Third, adding a geometric structure could protect relatively unstable components if any. For instance, Hu et al. encapsulated few layers of graphene on NiMo nanoparticles and improved its long-term stability in acidic medium. Their data showed that 3-5 graphene layers achieved the best balance between activity and stability.127 Fourth, using certain pretreatment processes to remove defects, dangling bonds, or surface oxides could also improve catalyst's stability. Ledendecker et al. found that by pretreating tungsten carbide (WC) with NaOH to remove native oxide layers, a significantly lower dissolution rate was observed at open circuit potential.128 Nevertheless, it is noteworthy that many defects and surface oxides also exhibit good catalytic

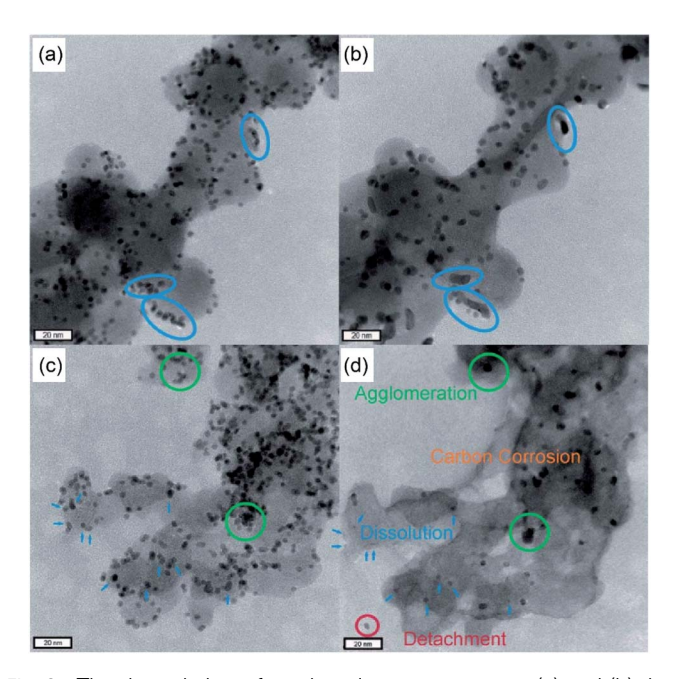


Fig. 8 The degradation of catalysts in measurements. (a) and (b) the images showing the migration and aggregation of Pt/C (a) before and (b) after 3600 cycles between 0.4 V and 1.4 V vs. RHE at a scan rate of 1 V s $^{-1}$  in 0.1 M HClO4. (c) and (d) the images showing four different degradation mechanisms of Pt/C (d) before and (d) after 3600 cycles between 0.4 V and 1.4 V vs. RHE at a scan rate of 1 V s $^{-1}$  in 0.1 M HClO4. Reprinted from ref. 31, copyright 2012, with permission from the Royal Society of Chemistry.

activities. Therefore, this strategy is somewhat a trade-off between activity and stability.

# 3. The power of coupling experiments with DFT for the HER

This section discusses the accomplishments made by coupling experiments and DFT in gaining insights into the fundamentals of the HER and facilitating the development of new HER electrocatalysts.

# 3.1. Insights into the fundamentals of the HER obtained from DFT

**3.1.1.** Explanation of experimental phenomena. DFT has been used to explain experimental results, for example, the pH dependence of H binding energy on the surface of Pt. The activity of Pt for catalyzing the HER in alkaline medium is two to three orders lower than that in acidic medium. <sup>83</sup> To explain the experimental observation, Cheng *et al.* employed *in situ* DFT calculation by taking the explicit solvent and potential into consideration and studied the H binding energy dependence over the Pt(100)/H<sub>2</sub>O interface. <sup>32</sup> As shown in Fig. 9, when pH increases from 0.2 to 12.8 at a potential of +0.3 V vs. RHE, it negatively shifts the potential from 0.29 V to -0.46 V vs. SHE. As a result, the adsorption of water on the surface was repelled, which in turn increased the adsorption energy of H on the surface of the electrode and consequently decreased the HER

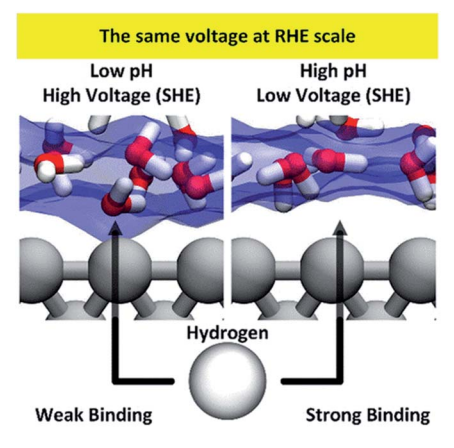


Fig. 9 The *in situ* quantum chemistry simulation of the pH dependence of the H binding energy over the  $Pt(100)/H_2O$  interface. Reprinted from ref. 32, copyright 2018, with permission from the American Chemistry Society.

activity. This work demonstrated the importance of considering water adsorption or surface hydrophilicity in the design of HER electrocatalysts.

3.1.2. Prediction of the reaction mechanism of the HER. It is noteworthy that the reaction mechanism of the HER is expected to be different for different materials. For example, Tang et al. studied the mechanism of the HER on the basal plane of 1T phase  $MoS_2$  by DFT and the calculated  $\Delta G_H^*$  indicated that the HER probably occurred with H coverage between 12.5-25%.33 The energy barrier calculation showed that under the H coverage of 25%, the Volmer step is fast with a small energy barrier of around 0.16 eV, while the Heyrovsky step (with an energy barrier of 0.62 eV) is preferred over the Tafel step (with a barrier of 1.07 eV). These values suggested that the HER proceeds via the Volmer-Heyrovsky reaction pathway, which is consistent with the measured Tafel slope of 40 mV dec<sup>-1</sup>. The authors also found that the HER activity of 1T phase MoS2 would increase when Mo was substituted by some other elements, like Mn, Ni, Fe, etc. Huang et al. performed the HER mechanistic study on the edge of 2H phase MoS2.35 They found that the HER took place via the Volmer-Heyrovsky pathway involving an electron-rich molybdenum hydride and a hydronium cation. The estimated energy barrier of 17.9 kcal  $\text{mol}^{-1}$  is in good agreement with the experimental value of 19.9 kcal mol<sup>-1</sup> estimated from turnover frequency (TOF). The protonation of the electron-rich Mo hydride is more favorable than the protonation of hydrogen on sulfur since the electron localized around the Mo-H bond is easier to transfer to form a H<sub>2</sub> bond. In the discussion of TMD HER catalysis, S-H has always been considered as an important intermediate. However, the authors found that the S-H bond was not a critical parameter for describing the HER activity since it did not play a direct role in determining the effective energy barrier. In contrast, the kinetic barriers, instead of equilibrium thermodynamics, are suggested to be the descriptor for evaluating the HER performance, which is supported by the consistency between the calculated and experimentally determined energy barriers.

Huang et al. also investigated the reaction mechanism of the HER on the basal plane sulfur vacancy site of 2H phase MoS<sub>2</sub> using grand canonical potential kinetics (GCP-K).34 Both the potential and pH dependence of the HER at the sulfur vacancy of the basal plane of 2H phase MoS<sub>2</sub> can be described by using the GCP-K formulation. The authors found that the ratedetermining step of the HER in both acidic and alkaline media was the Volmer step, in which the second H was adsorbed from the solution. The GCP-K formulation is able to show that the stretched bond distance changes continuously as a function of the applied potential, which explains the reason for the higher activity in the alkaline medium since the transition state (TS) is closer to the product, leading to a smaller Tafel slope of 60 mV dec<sup>-1</sup>. Their calculation results also suggested that the second H at the chalcogenide vacant site was the most active one. Based on that, the authors screened the rest of the 2H group VI TMD and found that MoTe<sub>2</sub> shows the most promising HER activity.

# 3.2. Development of new HER electrocatalysts facilitated by DFT

**3.2.1. TMDs.** TMDs are a well-studied class of materials for the HER due to their low cost and high efficiency.  $^{36,129}$  Hinnemann *et al.* found that natural enzymes, hydrogenase enzyme and nitrogenase enzyme, show high activity toward generating hydrogen. These enzymes have a favorable H adsorption activity compared to Pt, neither too weak nor too strong, with a  $\Delta G_{\rm H}^*$ 

value close to 0 (Fig. 10a). They used  $\Delta G_{\rm H}^*$  as the descriptor to screen and search for high performance electrocatalysts for the HER. The edges of  $MoS_2$  have a  $\Delta G_H^*$  value close to 0, suggesting its possible high activity toward the HER. This hypothesis was confirmed by the experimental results showing that MoS<sub>2</sub> deposited on graphite indeed had a reasonably good HER activity. Their work proved that  $\Delta G_H^*$  is a good descriptor for searching for HER electrocatalysts, and inspired others to work on MoS2. Although 2H phase MoS2 showed a decent activity for catalyzing the HER, it is still not comparable to Pt. The reasons include the poor conductivity, low density of active edge sites and low activity of the largely exposed basal planes of 2H phase MoS<sub>2</sub>. Therefore, a number of strategies such as improving the conductivity,40,130 maximizing the number of active edge sites36,42 and activating the inert basal planes of 2H phase MoS241,131,132 have been developed in the past 10 years to improve its HER performance. Among these strategies, here we would like to focus on the strategies of maximizing the number of edge sites and creating amorphous MoS2.

In order to investigate the active sites of 2H phase MoS<sub>2</sub>, Jaramillo *et al.* synthesized MoS<sub>2</sub> nanoplates on Au (111) using a physical vapor deposition method.<sup>42</sup> Fig. 10b shows the morphology of synthesized MoS<sub>2</sub> under a scanning tunneling microscope (STM). They found that the HER activity of MoS<sub>2</sub> is not proportional to the area of MoS<sub>2</sub> nanoplates. Instead, it is proportional to the edge length of MoS<sub>2</sub> (Fig. 10c and d), which suggests that the edges of 2H phase MoS<sub>2</sub> are the active sites for the HER. This pioneering work motivated a lot of follow up

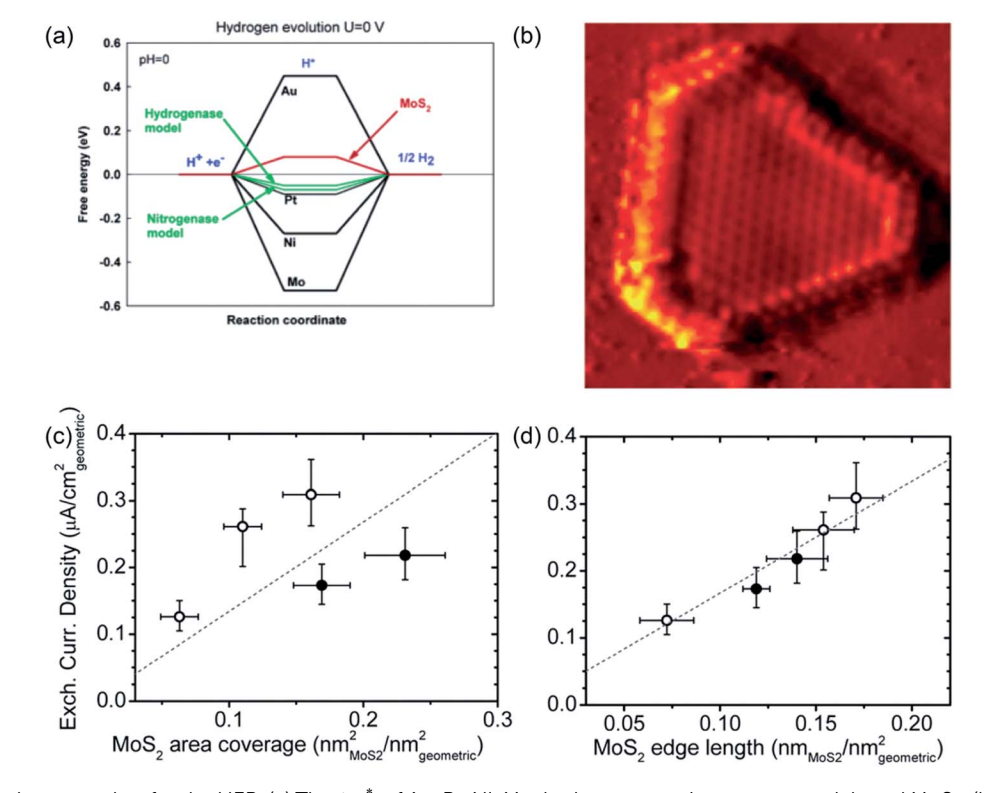


Fig. 10  $MoS_2$  as an electrocatalyst for the HER. (a) The  $\Delta G_H^*$  of Au, Pt, Ni, Mo, hydrogenase, nitrogenase models and  $MoS_2$ ; (b) the morphology of physical vapor deposited  $MoS_2$  under a STM; (c) and (d) the activity correlation of  $MoS_2$  with the (c) coverage area and (d) edge length. (a) Reprinted from ref. 36, copyright 2005, with permission from the American Chemistry Society. (b)–(d) Reprinted from ref. 42, copyright 2007, with permission from the American Association for the Advancement of Science.

studies to engineer the structure of MoS<sub>2</sub>, aiming to maximize the number of edge sites. For example, Kong et al. grew a vertically aligned MoS2 thin film on a substrate and exposed the maximum number of edge sites.56 Kibsgaard et al. reported a highly ordered double-gyroid MoS<sub>2</sub> structure with edge sites preferentially exposed, which showed high activity toward the HER.<sup>57</sup> Another approach to enhance the activity of MoS<sub>2</sub> is to synthesize an amorphous structure. 133 Defects are created in the structure when the long-range ordering in amorphous MoS2 is destroyed. Defect sites usually show good HER activity. For example, Vrubel et al. synthesized amorphous MoS2+x by electrodeposition. The amorphous MoS2+x achieved a current density of 20 mA cm<sup>-2</sup> at a small overpotential of 170 mV. <sup>134</sup> The undercoordinated S sites in amorphous MoS2+x are similar to the edge sites in crystalline 2H phase MoS<sub>2</sub> and are the possible active sites for catalyzing the HER.135

3.2.2. Carbon-based materials. Carbon-based materials are attractive HER catalysts due to their low cost and high abundance.136 Besides, compared to metal-based catalysts, they have better corrosion and oxidation resistivity, which is significant for practical applications. However, pristine carbon-based materials are known to be inert for the HER. Doping engineering methods have been reported to activate the catalytic activities of carbons under the guidance of DFT. DFT calculations revealed that by co-doping graphene with N and P atoms, the  $\Delta G_{\rm H}^*$  can be switched from a positive value to close to 0.136 Zheng et al. synthesized N and P co-doped graphene (N,P-G) and reported its HER performance. Obvious performance enhancement was observed for N,P-G compared to the undoped graphene sample. Since then, a number of follow-up studies of using doped carbon materials as HER electrocatalysts have been reported.37,137-139 For example, Zheng et al. also coupled graphitic-carbon nitride (g-C<sub>3</sub>N<sub>4</sub>) with nitrogen-doped graphene (NG).37 g-C3N4 has favorable H adsorption active sites, while the presence of NG facilitates charge transfer. The hybrid material achieved a current density of 10 mA cm<sup>-2</sup> at an overpotential of  $\sim$ 240 mV and a Tafel slope of 51.5 mV dec<sup>-1</sup>. These were the best values reported for carbon-based HER electrocatalysts at that time. Jiao et al. systematically investigated the role of different doping on the HER activity of carbon-based materials via a combination of DFT calculation, spectroscopic characterization, and electrochemical measurements. 139 The authors fitted the highest peak position  $(E_p)$  of DOS of the doped carbons with respect to  $\Delta G_{\rm H}^*$  and found that for a graphene surface, the higher the  $E_p$ , the more strongly the H is adsorbed on the surface. The interaction of H with the surface of graphene splits the hybridized energy states into two parts: the antibonding states, which usually cross the Fermi level, and the bonding states, which usually are below the Fermi level. The bonding strength of H on the surface is usually determined by the filling of the antibonding states. A higher energy of  $E_p$ means that the highest peak position is closer to the Fermi level, which moves up the antibonding states with a lower occupancy, stabilizing the bonding of H. Since the adsorption of H on the graphene surface is usually weak, the stronger bonding of H on the surface shifts  $\Delta G_{\rm H}^*$  closer to 0, corresponding to a higher activity. The  $\Delta G_{\rm H}^*$  of different dual heteroatom doped graphene

was well correlated with the experimental results, showing an activity order of N,S-G > N,P-G > N-G > N,B-G. Their work demonstrated that the activity of carbon-based materials can be boosted by tuning the electronic structure via rational heteroatom doping.

3.2.3. Single-atom catalysts. The concept of single-atom catalysts (SACs) is proposed because of the desire to achieve 100% utilization of metal atoms and reduce the cost of catalysts. Qiao et al. demonstrated the first synthesis of single-atom Pt anchored FeOx, denoted as Pt1/FeOx SAC, which showed a high activity for oxidizing CO.38 DFT calculations found that the charge transfer between Pt and FeOx made the Pt highly positive and gave it more vacant d orbitals, which stabilized the anchoring of Pt on FeOx and decreased the activation energy barrier for CO oxidation. SACs have been used for other catalytic reactions, like the HER, 25,140-142 ORR, 143-145 etc. Cheng et al. utilized the atomic layer deposition (ALD) method and successfully dispersed single platinum atoms and clusters onto N doped graphene nanosheets (NGNs).140 Single Pt anchored NGNs showed much higher activity and stability for the HER compared to the commercial Pt/C catalyst. DFT calculations indicated that the charge transfer induced partially unoccupied 5d orbitals of Pt are the reason for the extraordinary performance. Deng et al. reported single Pt atom doped MoS<sub>2</sub>, denoted as Pt/MoS2.141 DFT calculations revealed that the single atomic Pt doping can facilitate the adsorption of H on in-plane S sites neighboring to Pt sites. The authors also computed a series of different metal-doped MoS<sub>2</sub> systems and plotted a volcano based on their  $\Delta G_{\rm H}^*$  values, which was consistent with their experimental results on HER activity. Jiang et al. synthesized a nanoporous cobalt selenide with Co vacancies (denoted as np-Co<sub>0.85</sub>Se), which helped anchor single Pt in Co<sub>0.85</sub>Se (denoted as Pt/np-Co<sub>0.85</sub>Se) (Fig. 11).142 Pt/np-Co<sub>0.85</sub>Se showed a high HER activity in neutral medium. Operando XAS revealed a peak corresponding to the Co-OH bond forming under the working environment, suggesting that the single Pt doping can activate the nearby Co for H2O dissociation. DFT calculation revealed that Pt/np-Co<sub>0.85</sub>Se has a smaller H<sub>2</sub>O dissociation energy barrier of 0.491 eV, compared to np-Co<sub>0.85</sub>Se (0.881 eV). Additionally, Pt/np-Co<sub>0.85</sub>Se has more favorable H adsorption sites than Co<sub>0.85</sub>Se. The improved H adsorption and H<sub>2</sub>O dissociation together lead to a high HER activity.

3.2.4. MXenes. MXenes were first discovered by Naguib et al. and they got the name of MXenes because of their "graphene" like properties.146 MXenes are usually synthesized by exfoliating MAX with HF followed by sonication, among which M represents early transition metals, A represents mostly group 13 or 14 elements (Al or Ga), and X represents usually carbon or nitrogen. The first example of using MXenes as a HER electrocatalyst was reported by Seh et al.39 DFT calculation predicted that Mo<sub>2</sub>CT<sub>x</sub> is a promising HER electrocatalyst. First, the H adsorption energy of Mo<sub>2</sub>CT<sub>x</sub> is in a position closer to the top of the "Volcano plot". Second, the basal plane of two dimensional Mo<sub>2</sub>CT<sub>x</sub> was active for H adsorption, which is different from MoS2 whose edges are the active sites. Therefore, Mo<sub>2</sub>CT<sub>x</sub> has more active sites per unit area compared to that of MoS<sub>2</sub>. Two-dimensional MXenes have been used as

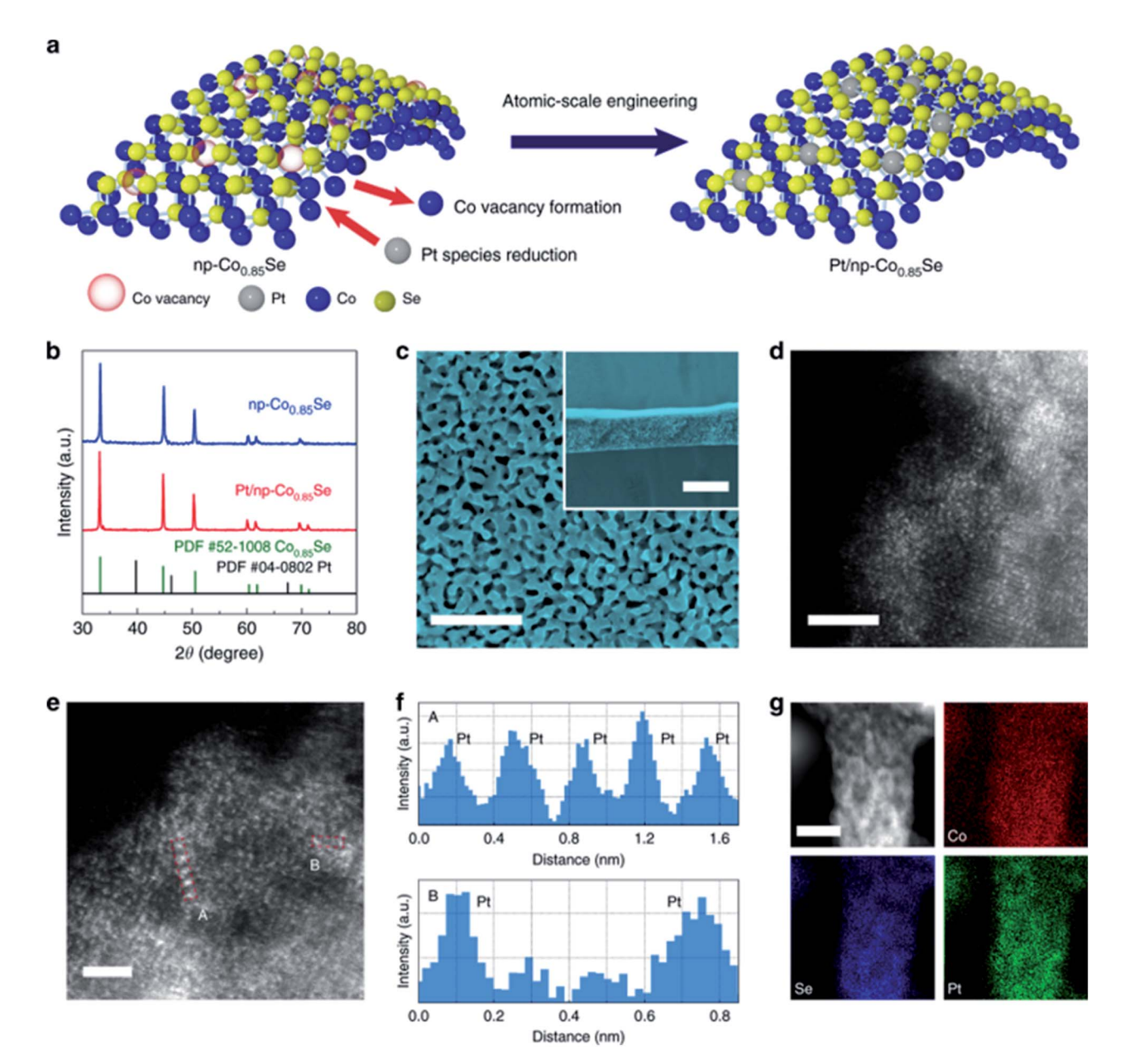


Fig. 11 The synthesis and characterization of Pt/np-Co<sub>0.85</sub>Se. (a) Schematic scheme of the synthesis procedures; (b) X-ray diffraction (XRD) of synthesized np- $Co_{0.85}$ Se and Pt/np- $Co_{0.85}$ Se; (c) scanning electron microscope (SEM) image of Pt/np- $Co_{0.85}$ Se and the inset shows the cross section of Pt/np-Co<sub>0.85</sub>Se; (d) and (e) HAADF-STEM images of Pt/np-Co<sub>0.85</sub>Se under different resolutions; (f) the line-scanning intensity profile obtained from the area highlighted by the red box in (e); (g) the scanning transmission electron microscopy-energy dispersive X-ray (STEM-EDX) mapping of Pt/np-Co<sub>0.85</sub>Se. Scale bar: c 500 nm; inset: 20 μm. (d) 2 nm. (e) 1 nm. (g) 10 nm. Reprinted from ref. 142, copyright 2019, with permission from Springer.

electrocatalysts for different reactions, including the HER, OER, ORR, etc. 44,147,148 Gao et al. employed DFT calculation to study a series of two-dimensional MXene materials and found that MXenes such as Ti<sub>2</sub>C, V<sub>2</sub>C, and Ti<sub>3</sub>C<sub>2</sub> are all conductive under standard conditions, which allows efficient charge transfer during the HER.44 Besides, the surface Pourbaix diagram indicated that MXenes are typically terminated by oxygen or hydroxyl groups, which have a favorable  $\Delta G_{\rm H}^*$  close to 0. Their computational work inspired numerous experimental studies on developing MXenes as HER electrocatalysts. 149,150 For example, Kuznetsov et al. synthesized a single Co doped 2D Mo<sub>2</sub>C structure (denoted as Mo<sub>2</sub>CT<sub>x</sub>:Co) that showed an excellent HER activity. EXAFS studies revealed that Co occupies the Mo sites and activates the terminated oxygen ions for H adsorption.149 Zhang et al. synthesized Mo2TiC2Tx with abundant exposed basal planes and Mo vacancies. 150 Mo vacancies help immobilize Pt atoms, and single Pt doped Mo<sub>2</sub>TiC<sub>2</sub>T<sub>x</sub> (denoted as Mo<sub>2</sub>TiC<sub>2</sub>T<sub>x</sub>-Pt<sub>SA</sub>) showed an impressive high mass activity, which is about 40 times higher than that of the commercial Pt/C catalyst. The DFT calculation unveiled that the

Table 1 HER performance of representative state-of-the-art HER electrocatalysts

Category	Catalyst	Electrolyte	$\eta$ (mV)@10 mA cm <sup>-2</sup>	Tafel slope (mV dec <sup>-1</sup> )
ТМО	$C-Ni_{1-x}O^{60}$	1.0 M KOH	27	36
	NiO/Ni-CNT <sup>155</sup>	1.0 M KOH	$\sim$ 90	~75
	NiO NRs-m-Ov <sup>156</sup>	1.0 M KOH	110	100
	Ni/NiO-250 (ref. 157)	1.0 M KOH	145	43
	Ni, Zn dual doped CoO <sup>158</sup>	1.0 M KOH	53	47
	Ni/NiO@C-2 (ref. 100)	1.0 M KOH	64	55
	NiO <sub>x</sub> @BCNTs <sup>159</sup>	1.0 M KOH	79	119
TMS	N doped $Ni_3S_2$ (ref. 69)	1.0 M KOH	155	113
	Ni <sub>3</sub> S <sub>2</sub> /NF <sup>160</sup>	1.0 M KOH	223	N/A
	Ni <sub>3</sub> S <sub>2</sub> (ref. 161) NiCo <sub>2</sub> S <sub>4</sub> /NF <sup>162</sup>	1.0 M KOH 1.0 M KOH	335 210	97 58 <b>.</b> 9
	Ni <sub>3</sub> S <sub>2</sub> NW <sup>163</sup>	1.0 M KOH	199	106.1
	N-NiS/MoS <sub>2</sub> (ref. 164)	1.0 M KOH	71	79
	MoNiS@NiS/CC <sup>165</sup>	0.5 M H <sub>2</sub> SO <sub>4</sub>	33	80
	A-RuS <sub>2</sub> (ref. 166)	0.5 M H <sub>2</sub> SO <sub>4</sub>	141	65.6
TMD	Porous MoS <sub>2</sub> film <sup>57</sup>	0.5 M H <sub>2</sub> SO <sub>4</sub>	150	50
	Single-layer MoS <sub>2</sub> (ref. 167)	0.5 M H <sub>2</sub> SO <sub>4</sub>	185	45
	SE-MoS <sub>2</sub> film <sup>168</sup>	$0.5 \text{ M H}_2\text{SO}_4$	104	59
	Monolayer MoS <sub>2</sub> (ref. 169)	0.5 M H <sub>2</sub> SO <sub>4</sub>	226	98
	$MoS_2@C^{170}$	0.5 M H <sub>2</sub> SO <sub>4</sub>	136	78
	Porous 1T MoS <sub>2</sub> NSs <sup>171</sup>	0.5 M H <sub>2</sub> SO <sub>4</sub>	153	43
	P-MoS <sub>2</sub> NSs <sup>172</sup>	$0.5 \text{ M H}_2\text{SO}_4$	43	34
	Ni-Co/1T-MoS <sub>2</sub> (ref. 173)	$0.5 \text{ M H}_2\text{SO}_4$	70	38
	1T MoSe <sub>2</sub> (ref. 174)	$0.5 \text{ M H}_2\text{SO}_4$	152	52
	MoSe <sub>2</sub> /SMCNT <sup>175</sup>	$0.5 \text{ M H}_2\text{SO}_4$	100	63
	B-MoSe <sub>2</sub> NSs <sup>176</sup>	$0.5 \text{ M H}_2\text{SO}_4$	84	39
	MoSSe nanodots <sup>177</sup>	$0.5 \text{ M H}_2\text{SO}_4$	140	80
	$1 \mathrm{T~WS_2~NSs}^{178}$	$0.5 \text{ M H}_2\text{SO}_4$	142	70
	$\text{Co-WS}_2/\text{W}_{18}\text{O}_{49}$ (ref. 179)	$0.5 \text{ M H}_2\text{SO}_4$	210	49
	FeS <sub>2</sub> -RGO film <sup>180</sup>	$0.5 \text{ M H}_2\text{SO}_4$	139	66
	$OGNs@MoS_2$ (ref. 181)	$0.5 \text{ M H}_2\text{SO}_4$	118	73
	$MoS_2/Ni_3S_2$ (ref. 182)	$0.5 \text{ M H}_2\text{SO}_4$	98	61
	Ni-Mo-S <sup>183</sup>	$0.5 \text{ M H}_2\text{SO}_4$	200	85
	$(\text{Fe}_x \text{Ni}_{1-x})_9 \text{S}_8 \text{ (ref. 184)}$	$0.5 \text{ M H}_2\text{SO}_4$	138	82
	FePSe <sub>3</sub> /NC <sup>185</sup>	$0.5 \text{ M H}_2\text{SO}_4$	70	53
Carbon-based materials	N,S-Doped graphene <sup>186</sup>	$0.5 \text{ M H}_2\text{SO}_4$	280	80.5
	EDA-CNTs <sup>187</sup>	0.5 M H <sub>2</sub> SO <sub>4</sub>	150	116
	N,P-Doped graphene <sup>136</sup>	0.5 M H <sub>2</sub> SO <sub>4</sub>	420	91
	N,P-Doped graphene <sup>136</sup> N,S-Doped CNT <sup>188</sup>	1.0 M KOH	480	145
	N,P-Doped C NWs <sup>189</sup>	1.0 M KOH	450 163	133 89
	3D graphene NWs <sup>59</sup>	$0.5 \text{ M H}_2\text{SO}_4$ $0.5 \text{ M H}_2\text{SO}_4$	107	64
	g-C <sub>3</sub> N <sub>4</sub> /graphene <sup>190</sup>	0.5 M H <sub>2</sub> SO <sub>4</sub>	207	54
	$C_3N_4$ (and $C_3N_4$ ) $C_3N_4$	0.5 M H <sub>2</sub> SO <sub>4</sub>	240	51.5
SACs	Pt-MoS <sub>2</sub> (ref. 141)	0.1 M H <sub>2</sub> SO <sub>4</sub>	~150	96
	400-SWMT/Pt <sup>191</sup>	0.5 M H <sub>2</sub> SO <sub>4</sub>	27	38
	PtSA-NT-NF <sup>192</sup>	1.0 M PBS	24	30
	Pt SAs/DG <sup>193</sup>	0.5 M H <sub>2</sub> SO <sub>4</sub>	23	25
	$Mo_2TiC_2T_x$ - $Pt_{SA}^{150}$	0.5 M H <sub>2</sub> SO <sub>4</sub>	30	30
	Pt@PCM <sup>194</sup>	0.5 M H <sub>2</sub> SO <sub>4</sub>	105	65.3
	Pt@PCM <sup>194</sup>	1.0 M KOH	139	73.6
	$Pt_1$ -MoO <sub>3-x</sub> (ref. 195)	$0.5 \text{ M H}_2\text{SO}_4$	23.3	28.8
	Pt SASs/AG <sup>196</sup>	0.5 M H <sub>2</sub> SO <sub>4</sub>	12	29.33
	SANi-PtNWs <sup>197</sup>	1.0 M KOH	70	60.3
	Pt/np-Co <sub>0.85</sub> Se <sup>142</sup>	1.0 M PBS	55	35
	Pd-MoS <sub>2</sub> (ref. 198)	$0.5 \text{ M H}_2\text{SO}_4$	78	62
	Pd/Cu-Pt NRs <sup>199</sup>	0.5 M H <sub>2</sub> SO <sub>4</sub>	22.8	25
	Ru SAs@PN <sup>200</sup>	0.5 M H <sub>2</sub> SO <sub>4</sub>	24	38
	Ru@Co SAs/N-C <sup>201</sup>	1.0 M KOH	7	30
	Pt–Ru dimer <sup>202</sup>	$0.5 \text{ M H}_2\text{SO}_4$	$\sim \! 20$	28.9
	$\mathrm{Fe/GD^{203}}$	$0.5 \text{ M H}_2\text{SO}_4$	66	37.8
	$ m Ni/GD^{203}$	0.5 M H <sub>2</sub> SO <sub>4</sub>	88	45.8
	A– $Ni$ – $C$ <sup>204</sup>	$0.5 \text{ M H}_2\text{SO}_4$	34	41

Table 1 (Contd.)

Category	Catalyst	Electrolyte	$\eta$ (mV)@10 mA cm $^{-2}$	Tafel slope (mV dec <sup>-1</sup> )
	Co-NG <sup>205</sup>	$0.5~\mathrm{M}~\mathrm{H_2SO_4}$	147	82
	Co1/PCN <sup>206</sup>	1.0 M KOH	138	52
	Co SAs/PTF-600 (ref. 207)	$0.5 \text{ M H}_2\text{SO}_4$	94	50
	$Mo_1N_1C_2$ (ref. 208)	$0.5 \text{ M H}_2\text{SO}_4$	154	86
	$W_1N_1C_3$ (ref. 209)	$0.5 \text{ M H}_2\text{SO}_4$	105	58
F-T O-T N-T Ti <sub>3</sub> Ni <sub>0</sub> Pt/T TBA Co- Mo	$Mo_2CT_x$ (ref. 151)	$0.5 \text{ M H}_2\text{SO}_4$	189	75
	F-Terminated $Ti_2CT_x$ (ref. 210)	$0.5 \text{ M H}_2\text{SO}_4$	170	100
	O-Terminated $Ti_2CT_x$ (ref. 211)	$0.5 \text{ M H}_2\text{SO}_4$	190	60.7
	$N-Ti_2CT_x$ (ref. 212)	$0.5 \text{ M H}_2\text{SO}_4$	215	67
	$Ti_3C_2T_x$ nanofibers <sup>213</sup>	$0.5 \text{ M H}_2\text{SO}_4$	169	97
	$Ni_{0.9}Co_{0.1}$ (a) Nb- $Ti_3C_2T_x$ (ref. 214)	1.0 M KOH	43.4	116
	$Pt/Ti_3C_2T_x$ -550 (ref. 215)	$0.1 \text{ M HClO}_4$	32.7	32.3
	$TBA-Ti_3C_2T_x-Pt-20$ (ref. 216)	$0.5 \text{ M H}_2\text{SO}_4$	70	65
	$Co-MoS_2@Mo_2CT_x$ (ref. 217)	1.0 M KOH	112	82
	$MoS_2 \perp Ti_3C_2$ (ref. 218)	$0.5 \text{ M H}_2\text{SO}_4$	110	${\sim}40$
	$Ni_{0.9}Fe_{0.1}PS_3$ (Ti <sub>3</sub> C <sub>2</sub> T <sub>x</sub> (ref. 219)	1.0 M KOH	196	114
	$MoS_2/Ti_3C_2$ -MXene@ $C^{220}$	$0.5 \text{ M H}_2\text{SO}_4$	135	45
	$Mo_2TiC_2T_x$ - $Pt_{SA}^{150}$	0.5 M H <sub>2</sub> SO <sub>4</sub>	30	30
	$CoP@3D Ti_3C_2T^{221}$	1.0 M KOH	168	58

favorable H adsorption activity on Mo<sub>2</sub>TiC<sub>2</sub>T<sub>x</sub>-Pt<sub>SA</sub> is the origin of its high HER activity.

The surface of MXenes has various possible terminations and, therefore, their properties are highly tunable. 151-154 For example, Handoko et al. combined both experimental and theoretical approaches to investigate the effect of 5 different basal plane functionalization (T<sub>r</sub>) on the HER activity. <sup>151</sup> They found that the higher the fluorine coverage on the basal plane, the lower the HER activity. Their results indicated that the oxygen terminations of MXenes are catalytically active toward the HER, which is different from the case of 2H phase TMDs such as MoS<sub>2</sub>, in which only the edge sites are active. The effect of transition metal modifications on the activity of M2XO2 was also studied by first principles screening.152 Li et al. found that although the majority of pristine MXenes showed a weak HER activity, transition metal surface modification can greatly enhance their HER activity. The presence of a transition metal not only optimizes  $\Delta G_{H}^{*}$  but also reduces the H<sub>2</sub> production activation barrier. A HER reaction mechanism switch from the Volmer-Heyrovsky pathway to the Volmer-Tafel pathway was observed after MXenes were modified with TM adatoms. A table (Table 1) summarizing the state-of-the-art HER electrocatalysts is listed below.

# 3.3. The limitations and progress of coupling experiments with DFT

Although significant research accomplishments have achieved, there are still challenges in coupling experiments with DFT. In this section, we will discuss the limitations and technical issues and review the progress made in the past few years.

#### 3.4. Experimental measurements

The measured "activity" of HER electrocatalysts could vary a lot depending on the experimental measurement conditions. Using a standardized measurement practice would be therefore critical for evaluating the catalyst's activity and making a fair comparison between the experimental and simulated results. For example, the overpotential required to achieve a geometric current density of 10 mA cm $^{-2}$  ( $\eta_{10}$ ) has often been used to compare the activity between different catalysts.  $\eta_{10}$  can be extracted from linear scan voltammetry (LSV). However, the current obtained from LSV includes two parts, faradaic current and capacitive current. As shown in the following equation, capacitive current increases with the scan rate:

$$\begin{split} I &= I_{\text{faradic}} + I_{\text{capacitive}} = I_{\text{faradic}} + \frac{\text{d}Q}{\text{d}t} = I_{\text{faradic}} + \frac{\text{d}Q}{\text{d}V} \frac{\text{d}V}{\text{d}t} \\ &= I_{\text{faradic}} + C \times (\text{scan rate}) \end{split} \tag{9}$$

The change of  $I_{\rm faradic}$  with the scan rate is small compared to that of  $I_{\rm capacitive}$  and, therefore,  $I_{\rm faradic}$  should be treated as a constant. Although the real system is better to be treated as a constant phase element (CPE) instead of a capacitive element,  $^{222}$  the above equation can still qualitatively explain why current increases with the scan rate. In order to minimize the effect of the scan rate and obtain the real faradaic current, it is recommended to measure the steady-state current with a dwell time of at least 5 minutes at different potentials.  $^{61}$ 

The determination and comparison of intrinsic activity between different HER electrocatalysts are imperative; however, they have rarely been reported in the literature. There are two ways to evaluate the intrinsic activity of electrocatalysts. First, instead of normalizing the current density (*j*) to the geometry surface area, *j* can be normalized to the mass of active catalysts or the electrochemical surface area (ECSA). These normalized current densities are called mass activity and specific activity, respectively (Fig. 12a). Depending on the structural features and mass loading of the catalyst, different metrics should be used to get a fair and accurate comparison. Among these

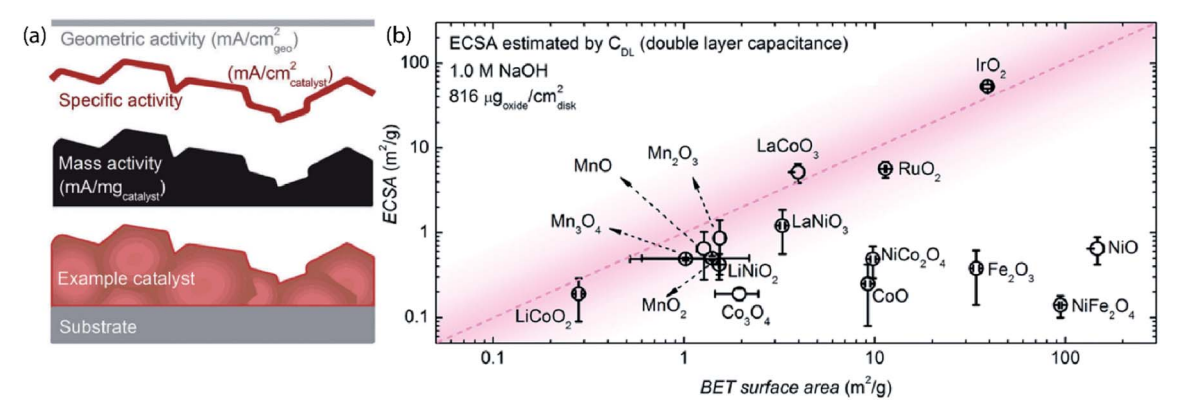


Fig. 12 A model of ECSA and different methods to calculate the ECSA. (a) Schematic picture showing the difference between geometry activity, specific activity, and mass activity. (b) The comparison between the C<sub>DL</sub>-estimated ECSAs of 16 metal oxide powders (assuming a specific capacitance of 40 μF cm<sub>oxide</sub>-2) and the surface areas measured by the Brunauer-Emmett-Teller (BET) method. Reprinted from ref. 45, copyright 2019, with permission from the American Chemistry Society.

methods, the value of the specific activity is determined by the ECSA, which is proportional to the total number of available active sites, which is a fair and accurate way to compare the intrinsic activity between different catalysts. The second way is to compare the catalyst's TOF, which is defined by the amount of the desired product (in the case of the HER, it is the H<sub>2</sub> molecule) catalyzed per active site per unit of time.<sup>61</sup> The key to calculating the specific activity and TOF is how to get a precise value of the ECSA. There are different methods to measure the ECSA such as the non-faradaic double layer capacitance  $(C_{DL})$ method, Brunauer-Emmett-Teller (BET) method, surface redox reactions method, etc.45 Among them, the CDL method is currently the most widely used for measuring the ECSA. The main uncertainty of using the  $C_{DL}$  method stems from the uncertainty in determining specific capacitance ( $C_{\text{spec}}$ ), a quantity which varies from one material to another. Even for the same material, different growth methods can sometimes lead to different  $C_{\rm spec}$  values. For example, the  $C_{\rm spec}$  of a (100)-oriented  $La_{0.6}Sr_{0.4}MnO_3$  thin-film was measured to be 77 µF cm<sup>-2</sup>, <sup>223</sup> which is higher than 40 μF cm<sup>-2</sup>, <sup>224</sup> a widely accepted value for metal oxides in the literature. Another uncertainty in the determination of  $C_{\text{spec}}$  is the possible current contributions from other side reactions (even in the non-faradaic reaction potential window) such as adsorption/desorption of H, intercalation, corrosion, etc.225 These side reactions may lead to overestimation of the double layer capacitive current. In addition, the electrical conductivity of the material can also affect the accuracy of the  $C_{\rm DL}$  method.<sup>226</sup> As shown in Fig. 12b, the ECSAs of 16 metal oxides measured by the  $C_{\rm DL}$  method are displayed and compared to the values obtained from BET measurement, a method based on physical adsorption of gas molecules on a solid surface. The results showed that the ECSAs of metal oxides with a high electrical conductivity, like IrO2, RuO2, LaNiO3 and LaCoO3, are pretty close to the values obtained from the BET method, while the ECSAs of those with poor electrical conductivity deviate significantly from the BET determined values. Therefore, it is important to know that the

CDL method is not perfect and should be used cautiously to measure the ECSA of electrocatalysts.

### 3.5. Characterization

Accurate structural information is the key to building accurate and reliable DFT models. Yet, most of the time catalysts are characterized in an environment that is different from the conditions in the catalytic reaction. As a result, inaccurate information could be obtained. To solve this problem, operando characterization techniques that can collect structural and activity/selection information during catalysis simultaneously have been developed. 227,228 They are powerful in determining the real active sites and correlating structure properties with catalytic activity. For example, Hu et al. observed that the catalytic activity of 2D nanosheets of a Ni-S coordination polymer was getting better during CV cycling (Fig. 13).229 The in situ XAS studies unveiled that the increased activity is because of the transformation of the Ni-S coordination polymer into an ultrathin Ni nanosheets with a trace amount of S adsorbed on the surface. Kornienko et al. used operando XANES and Raman spectroscopy to monitor the change of  $CoS_x$  during the HER process.230 They found that the CoSx catalyst was converted to a CoS<sub>2</sub>-like structure under cathodic potential. The high activity of  $CoS_x$  was believed to originate from the exposed S sites around those Co ions, which might establish different binding strength compared to the sites in bulk CoSx. Cao et al. used operando XAS to investigate the evolution of a single cobalt doped catalyst and confirmed the formation of a high-valence HO-Co1-N2 moiety due to the interaction between the Co-N4 structure and hydroxide.206 This HO-Co1-N2 structure could further interact with H2O molecules and serve as a H2O dissociation active site. The use of XAS helped identify the intrinsic active sites of this single cobalt doped catalyst. Casalongue et al. combined in situ ambient pressure X-ray photoelectron spectroscopy (APXPS) with DFT calculation and successfully determined the HER active sites of MoS<sub>3</sub>.<sup>231</sup> MoS<sub>3</sub> was gradually reduced to MoS2 during the HER process, accompanied by an activity enhancement, indicating that MoS2 was the active phase

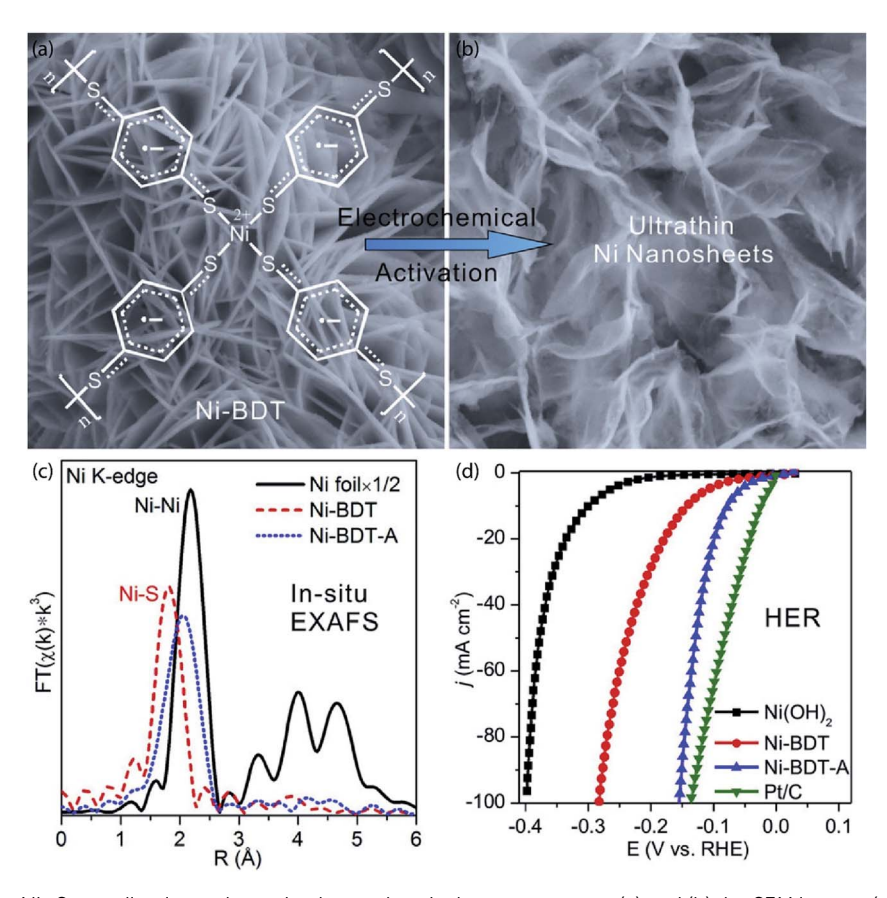


Fig. 13 The evolution of a Ni–S coordination polymer in electrochemical measurements. (a) and (b) the SEM images (a) before and (b) after HER measurements; (c) the EXAFS of reference (Ni foil) and Ni–DBT before and after electrochemical measurements; (d) LSV curves of Ni(OH)<sub>2</sub>, Ni–BDT, Ni–BDT-A, and Pt/C on a carbon cloth electrode in 1 M KOH (iR corrected). Reprinted from ref. 229, copyright 2017, with permission from Cell Press.

for the HER. Deng et al. reported operando Raman spectroscopy on amorphous MoS<sub>x</sub>.46 Under cathodic potential, a peak at 2530 cm<sup>-1</sup> corresponding to the S-H stretching vibration mode was observed in operando Raman spectroscopy (Fig. 14). In addition, the absence of Mo-H stretching mode excluded the possibility of Mo serving as an active site for the HER. Another interesting phenomenon observed under operando Raman spectroscopy was that the Raman signal of S-H stretching vibration mode appeared as early as +0.18 V vs. RHE, which indicated that the Volmer step (proton discharge step) occurred prior to the standard potential of H<sub>2</sub> evolution (0 V vs. RHE), but the adsorbed H didn't desorb from the surface in the form of H<sub>2</sub> until -0.15 V vs. RHE. It indicated that the H desorption step is the RDS, which is consistent with the experimentally measured Tafel slope of 40 mV dec<sup>-1</sup>. DFT calculation further showed that only non-apical S sites in the  $MoS_x$  structure were active for the HER. Another technique that has been used to probe the catalytic active sites is direct instrumental identification. For example, Jonas et al. employed an electrochemical scanning tunneling microscope (EC-STM) to study the HER on Pd islands covered an Au (111) surface.232 They observed the largest tunneling current on the boundary of Au and Pd, the smallest current on Au and intermediate current on the Pd surface. This is in good agreement with the fact that HER activity is higher on

the Pd islands deposited the Au (111) surface compared to the pure Au (111) surface and many layer Pd deposited Au (111) surface.

To summarize, these operando techniques, including XAS (XANES and EXAFS), XPS and Raman (or IR), are extremely useful in the determination of active sites and the catalytic

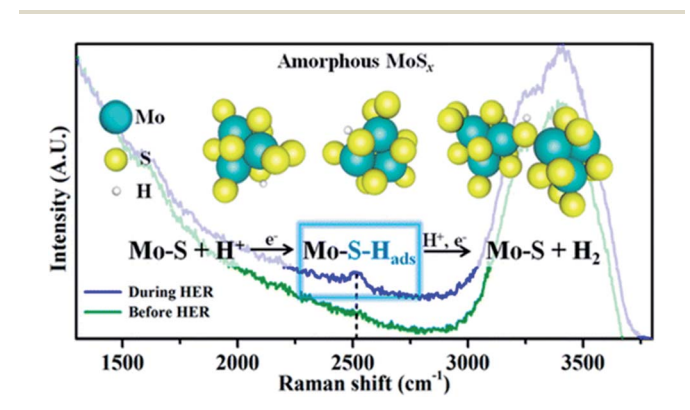


Fig. 14 The operando Raman spectroscopy of  $MoS_x$  in the HER. The peak around 2530 cm<sup>-1</sup> was assigned to the S–H stretching vibration mode. Reprinted from ref. 46, copyright 2016, with permission from the American Chemistry Society.

mechanism. Operando XANES is able to determine the oxidation states of the catalyst. 206 EXAFS analysis with proper fitting is able to investigate the coordination environment of the active sites in the material, including the coordination number and coordinating species. The challenge is to distinguish the signal from the bulk and surface of the catalyst. Operando APXPS is complementary to the XAS techniques since it extracts only the chemical information of the surface.231 Finally, if the catalyst contains X-H bonds, then operando Raman (or IR) spectroscopy would be highly favorable because of its high sensitivity to the vibrational mode of the X-H bond.46

#### 3.6. DFT simulation

The discussion of DFT simulation is elaborated from two aspects, the methodology development and the simulation of the electrolyte/electrode interface.

**3.6.1. Methodology of DFT.** The relatively low computation cost and reasonable accuracy for ground state properties make DFT outstanding and the most popular amongst all available electronic structure methods. However, the accuracy of the exchange-correlation (xc) functional is a recurring issue within the framework of DFT. In particular, there are many xc functionals, all of which vary in accuracy and computational expense. With new xc functionals being developed every year, it can be difficult to stay up-to-date. Here we briefly summarize a few studies to offer some perspective.

Commonly, xc functionals are either constructed from external parameter fitting of large databases ("empirical xc functionals") or from a rigorous theoretical framework with exact constraints ("nonempirical xc functionals"). For example, the revM06-L functional, which was optimized against a vast database with smoothness restraints, yields a mean unsigned error of 3.07 kcal mol<sup>-1</sup> for 422 chemical energies, offering a significant improvement over the previous implementation of M06-L.11 Another adaptation is the approach used by Hensley et al., wherein they implemented and weighted the sum of the energies from RPBE and optB, and found that they were able to yield accurate adsorption energies on transition metal surfaces.<sup>233</sup> On the other hand, these empirically fitted parameters can be a limitation of these xc functionals as they may rely on unrealistic error cancellation effects, which can be

fortuitous. These characteristics limit the generality and predictive power of standard xc functionals which can be highly system dependent. For example, Yungok et al. studied the xc functional dependence of H chemisorption thermodynamics with full consideration of binding energies, zero-point energy (ZPE) and vibrational entropy. It was found that the binding energy is the main factor determining the accuracy, but its predictive power is deteriorated by the high variability in the potential energy surface. On the other hand, the vibrational free energy of a weakly interacting van der Waals system showed a stronger xc functional dependence. Their discovery highlighted the importance of choosing the correct functional to provide a valid theoretical explanation and prediction.10,11,234,235

On the other hand, nonempirical xc functionals were developed by satisfying theoretical constraints and less dependent on the specific characteristics of systems. For example, a strongly constrained and appropriately normed (SCAN) semilocal density functional was constructed by enforcing 17 known exact constraints.236 This functional is more accurate than the GGAs PBE and PBEsol, at nearly the same computational cost. It was shown to give better barrier heights for 76 chemical reactions (BH76 set).237 However, its application in heterogeneous catalysis such as the HER has not been well validated so far. Other nonempirical xc functionals include Koopmanscompliant hybrid functionals<sup>238-241</sup> and dielectric-dependent hybrid functionals.242-245 The motivation of these functionals is to well describe the dielectric screening of solid-state systems and provide more accurate electronic structures. Therefore, they have been mostly used for predictions of bandgaps and band alignments instead of reaction energies or barriers.

In addition, advanced theoretical frameworks beyond DFT have been applied to heterogeneous catalysis, which include more accurate electron correlations such as the Random Phase Approximation (RPA), whose exchange treatment is exact and the correlation part is obtained from the linear density response function. Per et al. employed RPA to compute both the adsorption and surface energies of 10 surface reactions under a low coverage and found that it achieved a high accuracy compared to experimental data while DFT failed to describe either of them accurately (Fig. 15).246 Their study proved that RPA is a better and more universal total energy method for

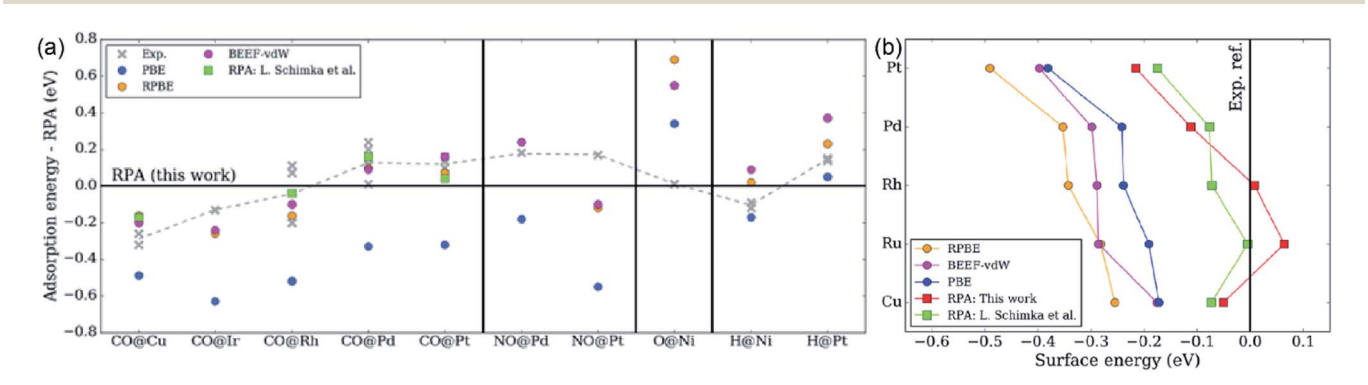


Fig. 15 Deviations of surface properties between RPA and other methods. (a) Adsorption energy and (b) surface energy calculated by RPA and other methods. Reprinted from ref. 246, copyright 2018, with permission from the American Chemistry Society

surface science, although it's more computationally demanding. They also employed RPA to calculate the adsorption database of 200 adsorption energies involving OH, CH, NO, CO, N2, N, O, and H over a wide range of 3d, 4d, and 5d transition metals, which showed a good consistency with a more advanced renormalized adiabatic LDA (rALDA) method, indicating the reliability and generality of RPA for adsorption and surface energy calculations. Another beyond-DFT method for catalysis applications is the multireference method that improves upon the single-particle approach of DFT-based methods. These methods include explicit arrangements of all electrons (i.e., electronic configurations) that are possible within a given user-defined spin and spatial symmetry.247 While this offers simulations of multi-electron catalysis processes, it is also limited by its greater computational expense.

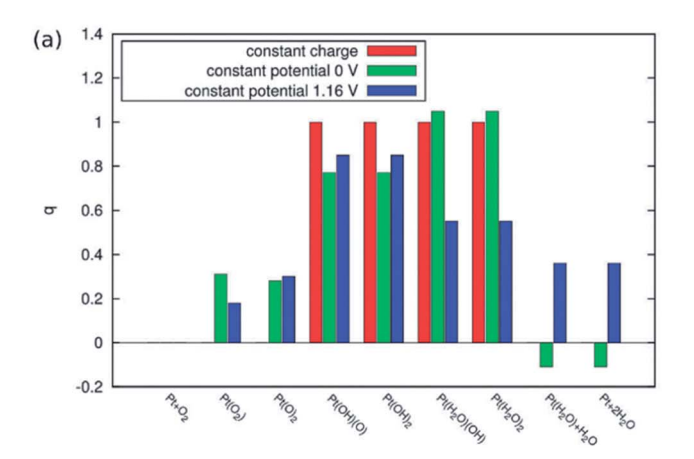
In summary, regardless of the method chosen, it is clear that a serious consideration of the balance between computational accuracy and computational expense must be made in the methodology-benchmarking process. We note that community-driven benchmarking can heighten the uniformity and clarify the choice of DFT-based methods.<sup>248</sup>

3.6.2. Simulation of the interface between the electrolyte and electrified electrode. The implementation of DFT calculation in electrocatalysis is very challenging since it has to not only describe the electronic structure of the catalyst but also simulate the electrode/electrolyte interface, which poses extra challenges for the implementation of DFT calculation in electrocatalysis.<sup>48</sup> In this section, the limitations and progress of including the effect of potential, solvent, solute, and pH in the computation will be discussed.

3.6.2.1. Potential. There are two different schemes to include the effect of potential, constant charge scheme and constant potential scheme. For the constant charge scheme, the number of electrons keeps constant, and there is no charge flow in or out of the system. In this scheme, the effect of potential is indirectly included by correcting the energy of the electrochemical step (*i.e.* the steps which have electron transfer) using qU, which means that potential doesn't have an effect on the

energy of the chemical step (i.e. the steps which don't have electron transfer). However, in reality, even if the step is a chemical step, potential still has an effect on its energy, which is not able to be reflected in the constant charge scheme. While for the constant potential scheme, potential has an effect on the chemical steps since electrons have to flow in or out of the system to keep the Fermi level fixed, which is closer to the realistic situation. 48,249 Fig. 16 shows the reaction pathway of the ORR on Pt, which clearly shows the difference between the constant charge scheme and constant potential scheme that there is only electron transfer for electrochemical steps in the constant charge scheme, but there is electron transfer for all steps in the constant potential scheme. Wang et al. also employed the constant potential scheme to simulate electric double-layer capacitors and they found that when the potential difference between two electrodes is large such as  $\Delta \Psi \ge 4 \text{ V}$ , the constant potential scheme showed a significant enhancement over the constant charge scheme of "inner-sphere adsorbed" Li ions very close to the electrode surface. The ability of the constant potential scheme being able to respond to local charge fluctuations in the electrolyte indicates that the constant potential scheme could reduce the energy/barrier for the approach of Li<sup>+</sup> ions to the electrode surface.<sup>250</sup>

3.6.2.2. Solvent. Since the solvent strongly affects the activity of electrocatalyst, it's necessary to include the effect of the solvent in the DFT calculation. There are two different approaches to simulate the effect of solvent, the explicit solvent model and the implicit solvent model.<sup>251</sup> The explicit solvation model is to include solvent molecules explicitly around the surface of the catalyst, and then these solvent molecules will be simulated together with a catalyst to reach thermodynamic equilibrium or compute free energy barriers based on *ab initio* MD as discussed earlier. The explicit solvent model can capture the hydrogen bond interaction, explicit charge transfer between the solvent and catalysts if any, a reasonable ion distribution and physical sampling of solvents.<sup>252</sup> However, the inclusion of a large number of solvent molecules required to capture the essential equilibrium properties and statistic averaging



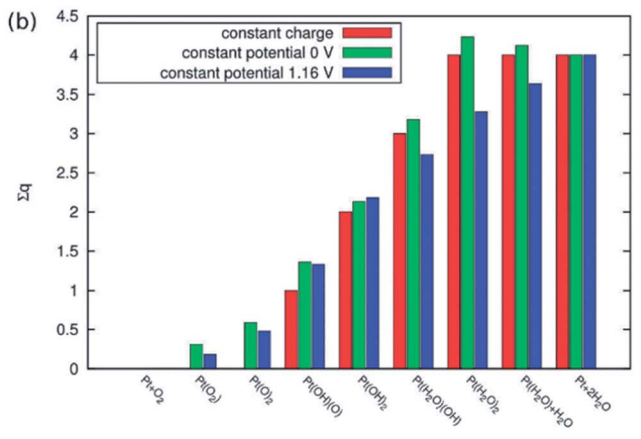


Fig. 16 The number of (a) transferred electrons in each step and (b) cumulative transferred electrons in all steps for the reaction pathway of the ORR on Pt calculated by using the constant charge and constant potential schemes. Reprinted from ref. 48, copyright 2013, with permission from the Royal Society of Chemistry.

substantially increases the computation cost. As a result, implicit solvent models or combined explicit few layers of water molecules with implicit solvent models remain popular.253 Instead, the implicit solvation model uses a homogeneously polarizable medium to simulate the effect of solvent molecules. Therefore, it is also called the continuum solvation model.<sup>254</sup> Several parameters need to be included in the construction of implicit solvent models, among which the dielectric constant is the most important because it represents the polarizability of the solvent. Compared to the explicit solvation model, the implicit solvation model can gain the long-range electrostatic effect of the solvent. Its disadvantage is that it cannot include the charge transfer process and physically resolve the local structure of the solvent.

There are two kinds of implicit solvation models, one involves the parametrization based on atomic radii while the other is based on solute electron density.53 The one based on atomic radii such as "SM" series and polarizable continuum models (PCMs)235,255,256 can be quite accurate for certain systems, but numerical problems which complicate the geometry optimization and MD calculation of the solute would be generated when it is extrapolated to new systems.<sup>53</sup> On the other hand, the solute electron density based implicit solvation model such as the self-consistent continuum solvation (SCCS) approach<sup>257,258</sup> uses a varying dielectric constant determined from the solute electron density, which avoids the numerical issues in atomic radii based models. Besides, density-based models require fewer parameters for the fitting, which makes them more reliable to extrapolate from one system to another system. However, the fewer parameters of density-based models also make them less accurate compared to atomic radii-based models. Especially for those charge asymmetric systems, density based models over solvate cations and under solvate anions.53 Sundararaman et al. developed a density-based implicit solvation model, which is able to handle the aforementioned charge asymmetric problem by including the cavity dependence on the solute electron density and potential. This new model is based on the charge-asymmetric nonlocally determined local electric response and referred to as the CANDLE solvation model.<sup>53</sup> As shown in Fig. 17, the CANDLE model shows a much better consistency with the experimental results compared to the linear PCM method and can reproduce solvation energies of neutral molecules, cations and anions with only a mean absolute error of 1.8 kcal mol<sup>-1</sup> in water and 3.0 kcal mol<sup>-1</sup> in acetonitrile.

3.6.2.3. Solute. The solute strongly affects the activity of the electrocatalyst, which has already been verified experimentally and theoretically. For example, Shinagawa et al. studied the effect of solute concentration on the ORR and HOR on Pt in a buffered solution.259 It was found that a higher concentration of solute decreased the gas solubility and increased the kinematic viscosity of the solution and the diffusion coefficient of the dissolved gas. Pham et al. studied the electronic structure of an aqueous liquid by a combination of first principles methods, experimental verification, and spectroscopic measurements.54 By using a dielectric hybrid functional and range-separated hybrid (RSH) and self-consistent hybrid (sc-hybrid)

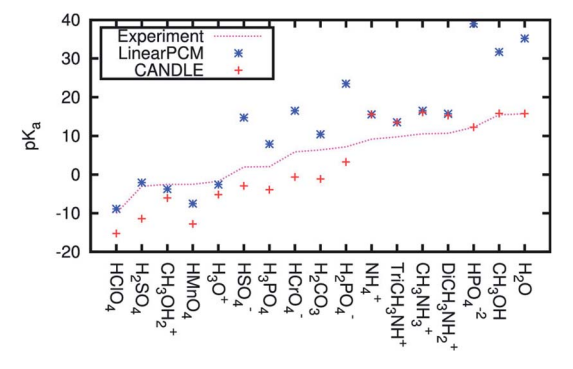


Fig. 17 Acid dissociation constant ( $pK_a$ ) of different molecules and ions in H<sub>2</sub>O predicted by using the CANDLE model and linear PCM method compared to that of the experiment. Reprinted from ref. 53, copyright 2015, with permission from the American Institute of Physics.

functionals, the ionization potentials (IPs) of 16 solvated anions can be accurately captured and were comparable to the experimental data. Besides, the proposed computational framework can also be applied to other liquids, which proved the generality of the method and paved the way for understanding and engineering the electrolyte for different energy conversion and storage techniques.

3.6.2.4. pH. The activity of an electrocatalyst strongly depends on the pH of the electrolyte. A good example is that the HER activity of Pt in alkaline medium is two to three orders lower than that in acidic medium.83 One approach to simulate the effect of pH is to convert the pH effect to the potential effect. For example, Cheng et al. studied the pH dependence of H binding energy on Pt(100)/H2O and a pH change from 0.2 to 12.8 at U = +0.3 V (vs. RHE) was converted to a potential change from +0.29 to -0.46 V on the SHE scale by using the Nernst equation.32 However, this conversion is only applicable for surfaces on which H<sup>+</sup> and OH<sup>-</sup> are the only charge determining ions.260-262 Another approach to simulate the effect of pH is to correlate pH at the point of zero charge (pHZPC) with the

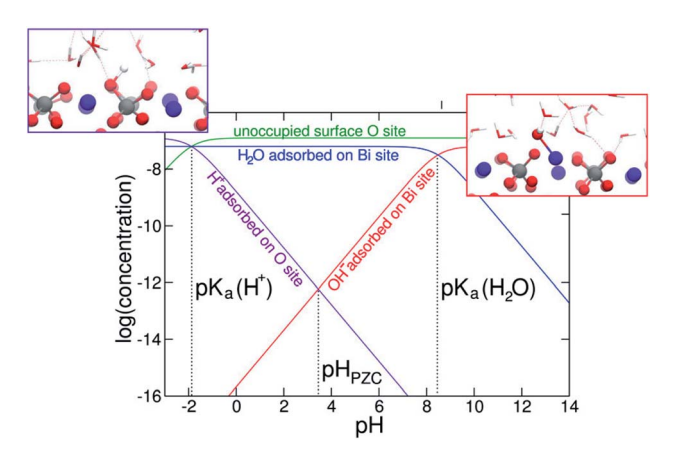


Fig. 18 The pH-dependent surface chemistry of the BiVO<sub>4</sub>(010)water interface. Reprinted from ref. 55, copyright 2018, with permission from the American Chemical Society.

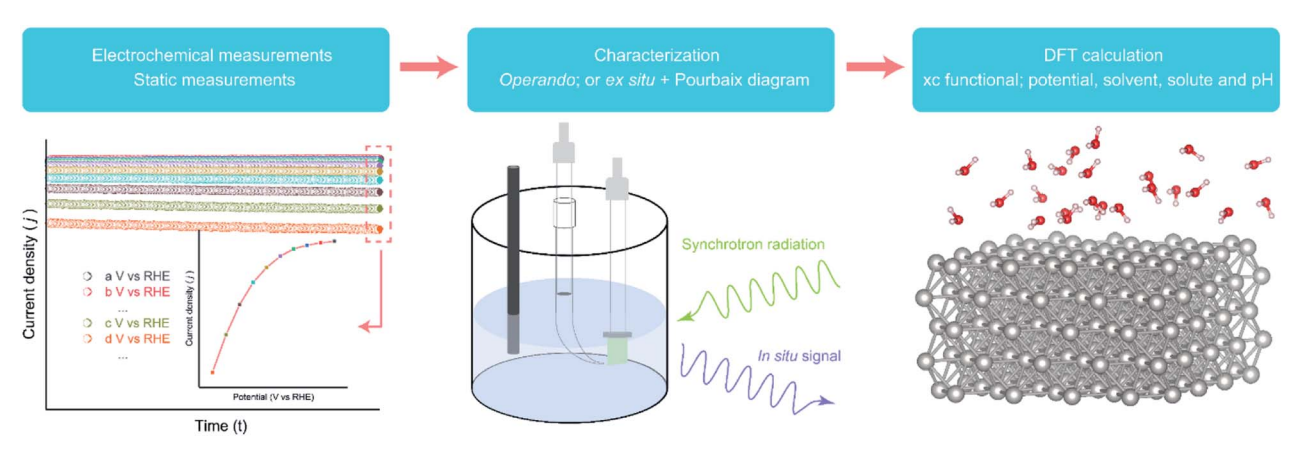


Fig. 19 A schematic illustration of coupling experiments with DFT calculation.

chemical potential of an isolated proton. Ambrosio et al. used this method to study the pH dependence surface chemistry over a BiVO<sub>4</sub> (010)-water interface by supplementing electronic structure calculation, MD calculation, and the thermodynamic integration method together. 55 A pH dependence diagram of the BiVO<sub>4</sub> (010) surface in an aqueous environment was plotted via the h-rVV10 level of theory, finding that protons, H<sub>2</sub>O molecules, and hydroxide ions are the dominant adsorbates under strong acidic conditions, pH ranging from 2 to 8, and pH larger than 8.2, respectively (Fig. 18).

### Summary and outlook

Integrating experimental and computational efforts has been proven to be highly effective in moving forward in the field of electrocatalysis. In this article, we have reviewed the recent accomplishments, developments, and limitations in implementing DFT for studying HER catalysts. Here we would like to share some suggestions on the coupling of experiments and DFT calculation (Fig. 19). First, in order to improve consistency between experimental and simulation results, the catalytic system has to be well defined and it should be as simple as possible. A complicated structure consisting of different phases and defects would create too many possibilities and rapidly increase the computational cost. A single crystal system would be preferred from a computational perspective. Second, experimental measurements should be carefully performed, for example, using steady current instead of the current obtained from LSV, minimizing mass diffusion limitation via rotating the electrodes and/or using ordered porous structures, and accurately measuring the ECSA for determining accurate intrinsic activities. Third, it is important to use the correct and accurate structural information to build the DFT model. Operando techniques are highly preferred in probing the structural information of the catalyst under the working environment.161 If in situ measurements are impossible, then the structural information of the catalyst should be collected at least before and after the electrochemical measurements to verify any possible structural changes during the reaction. The surface Pourbaix diagram is recommended to be calculated given the

thermodynamically most stable phase and surface termination varies under different pH and potential conditions. 156 Finally, to perform DFT calculation closer to the real working conditions, xc functionals have to be carefully chosen. In certain cases, it is recommended to use higher level total energy calculation methods, such as RPA, to compute desired quantities. Furthermore, correctly and accurately simulating the interface between the electrolyte and electrified electrode is critical for understanding the catalytic reactions. Factors, including potential, solute, solvent and pH, should be carefully considered. Although numerous methods have been developed to simulate these effects, each method has its limitations. For example, the implicit solvation model is not able to capture the charge transfer process and physically resolve the local structure of the solvent. Therefore, new methods have to be developed to tackle these issues. We believe that the seamless coupling between experiments and DFT calculation can deepen the understanding of catalytic mechanisms of different catalysts and accelerate the development of new electrocatalysts for different reactions and conditions.

### Conflicts of interest

There are no conflicts of interest to declare.

### Acknowledgements

Y. P. acknowledges the support of the National Science Foundation under Grants No. DMR-1760260 and No. CHE-1904547. Y. L. acknowledges the financial support from the Merced nAnomaterials Center for Energy and Sensing (MACES), a NASA funded MIRO center, under award NNX15AQ01.

### References

- 1 L. Barreto, A. Makihira and K. Riahi, Int. J. Hydrogen Energy, 2003, 28, 267-284.
- 2 F. Mueller-Langer, E. Tzimas, M. Kaltschmitt and S. Peteves, Int. J. Hydrogen Energy, 2007, 32, 3797-3810.

- 3 R. Ramachandran and R. K. Menon, *Int. J. Hydrogen Energy*, 1998, **23**, 593–598.
- 4 W. C. Lattin and V. P. Utgikar, Int. J. Hydrogen Energy, 2007, 32, 3230–3237.
- 5 M. Z. Jacobson, W. G. Colella and D. M. Golden, *Science*, 2005, 308, 1901.
- 6 D. L. Trimm and Z. I. Önsan, Catal. Rev., 2001, 43, 31-84.
- 7 J. M. Ogden, Annu. Rev. Energy, 1999, 24, 227–279.
- 8 S. Satyapal, J. Petrovic, C. Read, G. Thomas and G. Ordaz, *Catal. Today*, 2007, **120**, 246–256.
- 9 Z. W. Seh, J. Kibsgaard, C. F. Dickens, I. Chorkendorff, J. K. Nørskov and T. F. Jaramillo, *Science*, 2017, 355, eaad4998.
- 10 Y. Zhao and D. G. Truhlar, *J. Chem. Theory Comput.*, 2011, 7, 669–676.
- 11 Y. Wang, X. Jin, H. S. Yu, D. G. Truhlar and X. He, *Proc. Natl. Acad. Sci.*, 2017, **114**, 8487.
- 12 P. J. Hasnip, K. Refson, M. I. J. Probert, J. R. Yates, S. J. Clark and C. J. Pickard, *Philos. Trans. R. Soc.*, A, 2014, 372, 20130270.
- 13 N. Mardirossian and M. Head-Gordon, *Mol. Phys.*, 2017, 115, 2315–2372.
- 14 B. Hammer, L. B. Hansen and J. K. Nørskov, *Phys. Rev. B*, 1999, **59**, 7413–7421.
- 15 J. K. Nørskov, F. Abild-Pedersen, F. Studt and T. Bligaard, *Proc. Natl. Acad. Sci.*, 2011, **108**, 937.
- 16 Top 500, https://www.top500.org/lists/2019/11/, Nov, 2019.
- 17 D. R. Bowler, J. S. Baker, J. T. L. Poulton, S. Y. Mujahed, J. Lin, S. Yadav, Z. Raza and T. Miyazaki, *Jpn. J. Appl. Phys.*, 2019, **58**, 100503.
- 18 A. Erba, J. Baima, I. Bush, R. Orlando and R. Dovesi, *J. Chem. Theory Comput.*, 2017, 13, 5019–5027.
- 19 W. Hu, L. Lin and C. Yang, J. Chem. Phys., 2015, 143, 124110.
- 20 S. Niu, Y. Fang, J. Zhou, J. Cai, Y. Zang, Y. Wu, J. Ye, Y. Xie, Y. Liu, X. Zheng, W. Qu, X. Liu, G. Wang and Y. Qian, J. Mater. Chem. A, 2019, 7, 10924–10929.
- 21 S. Liu, C. Chen, Y. Zhang, Q. Zheng, S. Zhang, X. Mu, C. Chen, J. Ma and S. Mu, J. Mater. Chem. A, 2019, 7, 14466–14472.
- 22 M. Mavrikakis, B. Hammer and J. K. Nørskov, *Phys. Rev. Lett.*, 1998, **81**, 2819–2822.
- 23 Y. Zang, S. Niu, Y. Wu, X. Zheng, J. Cai, J. Ye, Y. Xie, Y. Liu, J. Zhou, J. Zhu, X. Liu, G. Wang and Y. Qian, *Nat. Commun.*, 2019, 10, 1217.
- 24 R. Subbaraman, D. Tripkovic, D. Strmenik, K.-C. Chang, M. Uchimura, A. P. Paulikas, V. Stamenkovic and N. M. Markovic, *Science*, 2011, 334, 1256.
- 25 Y. Zheng, Y. Jiao, A. Vasileff and S.-Z. Qiao, *Angew. Chem.*, *Int. Ed.*, 2018, **57**, 7568–7579.
- 26 D. Wang, X. Zhang, S. Bao, Z. Zhang, H. Fei and Z. Wu, J. Mater. Chem. A, 2017, 5, 2681–2688.
- 27 D. Malevich, E. Halliop, B. A. Peppley, J. G. Pharoah and K. Karan, *J. Electrochem. Soc.*, 2009, **156**, B216–B224.
- 28 Z. Lu, W. Zhu, X. Yu, H. Zhang, Y. Li, X. Sun, X. Wang, H. Wang, J. Wang, J. Luo, X. Lei and L. Jiang, *Adv. Mater.*, 2014, 26, 2683–2687.

- 29 J. Hao, W. Yang, Z. Huang and C. Zhang, *Adv. Mater. Interfaces*, 2016, 3, 1600236.
- 30 J. C. Meier, C. Galeano, I. Katsounaros, A. A. Topalov, A. Kostka, F. Schüth and K. J. J. Mayrhofer, *ACS Catal.*, 2012, 2, 832–843.
- 31 J. C. Meier, I. Katsounaros, C. Galeano, H. J. Bongard, A. A. Topalov, A. Kostka, A. Karschin, F. Schüth and K. J. J. Mayrhofer, *Energy Environ. Sci.*, 2012, 5, 9319–9330.
- 32 T. Cheng, L. Wang, B. V. Merinov and W. A. Goddard, *J. Am. Chem. Soc.*, 2018, **140**, 7787–7790.
- 33 Q. Tang and D.-e. Jiang, ACS Catal., 2016, 6, 4953-4961.
- 34 Y. Huang, R. J. Nielsen and W. A. Goddard, *J. Am. Chem. Soc.*, 2018, **140**, 16773–16782.
- 35 Y. Huang, R. J. Nielsen, W. A. Goddard and M. P. Soriaga, *J. Am. Chem. Soc.*, 2015, **137**, 6692–6698.
- 36 B. Hinnemann, P. G. Moses, J. Bonde, K. P. Jørgensen, J. H. Nielsen, S. Horch, I. Chorkendorff and J. K. Nørskov, J. Am. Chem. Soc., 2005, 127, 5308–5309.
- 37 Y. Zheng, Y. Jiao, Y. Zhu, L. H. Li, Y. Han, Y. Chen, A. Du, M. Jaroniec and S. Z. Qiao, *Nat. Commun.*, 2014, 5, 3783.
- 38 B. Qiao, A. Wang, X. Yang, L. F. Allard, Z. Jiang, Y. Cui, J. Liu, J. Li and T. Zhang, *Nat. Chem.*, 2011, 3, 634.
- 39 Z. W. Seh, K. D. Fredrickson, B. Anasori, J. Kibsgaard, A. L. Strickler, M. R. Lukatskaya, Y. Gogotsi, T. F. Jaramillo and A. Vojvodic, ACS Energy Lett., 2016, 1, 589–594.
- 40 M. A. Lukowski, A. S. Daniel, F. Meng, A. Forticaux, L. Li and S. Jin, *J. Am. Chem. Soc.*, 2013, 135, 10274–10277.
- 41 H. Li, C. Tsai, A. L. Koh, L. Cai, A. W. Contryman, A. H. Fragapane, J. Zhao, H. S. Han, H. C. Manoharan, F. Abild-Pedersen, J. K. Nørskov and X. Zheng, *Nat. Mater.*, 2016, **15**, 48–53.
- 42 T. F. Jaramillo, K. P. Jørgensen, J. Bonde, J. H. Nielsen, S. Horch and I. Chorkendorff, *Science*, 2007, 317, 100.
- 43 C. Choi, S. Back, N.-Y. Kim, J. Lim, Y.-H. Kim and Y. Jung, *ACS Catal.*, 2018, **8**, 7517–7525.
- 44 G. Gao, A. P. O'Mullane and A. Du, *ACS Catal.*, 2017, 7, 494–500.
- 45 C. Wei, S. Sun, D. Mandler, X. Wang, S. Z. Qiao and Z. J. Xu, *Chem. Soc. Rev.*, 2019, **48**, 2518–2534.
- 46 Y. Deng, L. R. L. Ting, P. H. L. Neo, Y.-J. Zhang, A. A. Peterson and B. S. Yeo, ACS Catal., 2016, 6, 7790–7798.
- 47 V. I. Anisimov, J. Zaanen and O. K. Andersen, *Phys. Rev. B*, 1991, **44**, 943–954.
- 48 U. Benedikt, W. B. Schneider and A. A. Auer, *Phys. Chem. Chem. Phys.*, 2013, **15**, 2712–2724.
- 49 Y. Ping, R. J. Nielsen and W. A. Goddard, *J. Am. Chem. Soc.*, 2017, **139**, 149–155.
- 50 T. Cheng, H. Xiao and W. A. Goddard, *Proc. Natl. Acad. Sci.*, 2017, **114**, 1795.
- 51 T. Cheng, H. Xiao and W. A. Goddard, *J. Am. Chem. Soc.*, 2016, **138**, 13802–13805.
- 52 H. Xiao, T. Cheng and W. A. Goddard, *J. Am. Chem. Soc.*, 2017, **139**, 130–136.
- 53 R. Sundararaman and W. A. Goddard, *J. Chem. Phys.*, 2015, **142**, 064107.

- 54 T. A. Pham, M. Govoni, R. Seidel, S. E. Bradforth, E. Schwegler and G. Galli, *Sci. Adv.*, 2017, 3, e1603210.
- 55 F. Ambrosio, J. Wiktor and A. Pasquarello, *ACS Appl. Mater. Interfaces*, 2018, **10**, 10011–10021.
- 56 D. Kong, H. Wang, J. J. Cha, M. Pasta, K. J. Koski, J. Yao and Y. Cui, *Nano Lett.*, 2013, 13, 1341–1347.
- 57 J. Kibsgaard, Z. Chen, B. N. Reinecke and T. F. Jaramillo, *Nat. Mater.*, 2012, **11**, 963–969.
- 58 Y. Wu, X. Liu, D. Han, X. Song, L. Shi, Y. Song, S. Niu, Y. Xie, J. Cai, S. Wu, J. Kang, J. Zhou, Z. Chen, X. Zheng, X. Xiao and G. Wang, *Nat. Commun.*, 2018, 9, 1425.
- 59 H. Wang, X.-B. Li, L. Gao, H.-L. Wu, J. Yang, L. Cai, T.-B. Ma, C.-H. Tung, L.-Z. Wu and G. Yu, *Angew. Chem., Int. Ed.*, 2018, 57, 192–197.
- 60 T. Kou, M. Chen, F. Wu, T. J. Smart, S. Wang, Y. Wu, Y. Zhang, S. Li, S. Lall, Z. Zhang, Y.-S. Liu, J. Guo, G. Wang, Y. Ping and Y. Li, *Nat. Commun.*, 2020, 11, 590.
- 61 X. Zou and Y. Zhang, Chem. Soc. Rev., 2015, 44, 5148-5180.
- 62 M. R. G. de Chialvo and A. C. Chialvo, *J. Electroanal. Chem.*, 1994, 372, 209–223.
- 63 M. R. Gennero de Chialvo and A. C. Chialvo, *Electrochim. Acta*, 1998, 44, 841–851.
- 64 K. Zeng and D. Zhang, Prog. Energy Combust. Sci., 2010, 36, 307–326.
- 65 J. Greeley, T. F. Jaramillo, J. Bonde, I. Chorkendorff and J. K. Nørskov, *Nat. Mater.*, 2006, 5, 909–913.
- 66 Q. Zhang, D. Q. Lima, I. Lee, F. Zaera, M. Chi and Y. Yin, *Angew. Chem., Int. Ed.*, 2011, **50**, 7088–7092.
- 67 H. Wang, C. Tsai, D. Kong, K. Chan, F. Abild-Pedersen, J. K. Nørskov and Y. Cui, *Nano Res.*, 2015, **8**, 566–575.
- 68 D.-Y. Wang, M. Gong, H.-L. Chou, C.-J. Pan, H.-A. Chen, Y. Wu, M.-C. Lin, M. Guan, J. Yang, C.-W. Chen, Y.-L. Wang, B.-J. Hwang, C.-C. Chen and H. Dai, *J. Am. Chem. Soc.*, 2015, 137, 1587–1592.
- 69 T. Kou, T. Smart, B. Yao, I. Chen, D. Thota, Y. Ping and Y. Li, Adv. Energy Mater., 2018, 8, 1703538.
- 70 P. Raybaud, J. Hafner, G. Kresse, S. Kasztelan and H. Toulhoat, *J. Catal.*, 2000, **189**, 129–146.
- 71 T. Zheng, W. Sang, Z. He, Q. Wei, B. Chen, H. Li, C. Cao, R. Huang, X. Yan, B. Pan, S. Zhou and J. Zeng, *Nano Lett.*, 2017, 17, 7968–7973.
- 72 J. R. Kitchin, J. K. Nørskov, M. A. Barteau and J. G. Chen, *Phys. Rev. Lett.*, 2004, **93**, 156801.
- 73 M. Luo and S. Guo, Nat. Rev. Mater., 2017, 2, 17059.
- 74 D. Voiry, H. Yamaguchi, J. Li, R. Silva, D. C. B. Alves, T. Fujita, M. Chen, T. Asefa, V. B. Shenoy, G. Eda and M. Chhowalla, *Nat. Mater.*, 2013, 12, 850–855.
- 75 B. Hammer and J. K. Norskov, *Nature*, 1995, 376, 238-240.
- 76 J. Greeley, J. K. Nørskov and M. Mavrikakis, *Annu. Rev. Phys. Chem.*, 2002, 53, 319–348.
- 77 K. Sakmann, A. I. Streltsov, O. E. Alon and L. S. Cederbaum, Phys. Rev. Lett., 2009, 103, 220601.
- 78 K. Yan, T. A. Maark, A. Khorshidi, V. A. Sethuraman, A. A. Peterson and P. R. Guduru, *Angew. Chem., Int. Ed.*, 2016, 55, 6175–6181.
- 79 Y. Jiao, Y. Zheng, M. Jaroniec and S. Z. Qiao, *Chem. Soc. Rev.*, 2015, 44, 2060–2086.

- 80 A. Vojvodic, A. Hellman, C. Ruberto and B. I. Lundqvist, *Phys. Rev. Lett.*, 2009, **103**, 146103.
- 81 Z. Li, J. Fu, Y. Feng, C. Dong, H. Liu and X. Du, *Nat. Catal.*, 2019, 2, 1107–1114.
- 82 L. Wang, Z. Zeng, W. Gao, T. Maxson, D. Raciti, M. Giroux, X. Pan, C. Wang and J. Greeley, *Science*, 2019, 363, 870.
- 83 W. Sheng, H. A. Gasteiger and Y. Shao-Horn, *J. Electrochem. Soc.*, 2010, 157, B1529–B1536.
- 84 R. Subbaraman, D. Tripkovic, K.-C. Chang, D. Strmcnik, A. P. Paulikas, P. Hirunsit, M. Chan, J. Greeley, V. Stamenkovic and N. M. Markovic, *Nat. Mater.*, 2012, **11**, 550–557.
- 85 D. Strmenik, M. Uchimura, C. Wang, R. Subbaraman, N. Danilovic, D. van der Vliet, A. P. Paulikas, V. R. Stamenkovic and N. M. Markovic, *Nat. Chem.*, 2013, 5, 300–306.
- 86 J. Zheng, W. Sheng, Z. Zhuang, B. Xu and Y. Yan, *Sci. Adv.*, 2016, 2, e1501602.
- 87 E. Liu, J. Li, L. Jiao, H. T. T. Doan, Z. Liu, Z. Zhao, Y. Huang, K. M. Abraham, S. Mukerjee and Q. Jia, *J. Am. Chem. Soc.*, 2019, 141, 3232–3239.
- 88 N. Ramaswamy, S. Ghoshal, M. K. Bates, Q. Jia, J. Li and S. Mukerjee, *Nano Energy*, 2017, **41**, 765–771.
- 89 S. Intikhab, J. D. Snyder and M. H. Tang, *ACS Catal.*, 2017, 7, 8314–8319.
- B. L. Trout and M. Parrinello, J. Phys. Chem. B, 1999, 103, 7340–7345.
- 91 Y.-C. Hao, Y. Guo, L.-W. Chen, M. Shu, X.-Y. Wang, T.-A. Bu, W.-Y. Gao, N. Zhang, X. Su, X. Feng, J.-W. Zhou, B. Wang, C.-W. Hu, A.-X. Yin, R. Si, Y.-W. Zhang and C.-H. Yan, *Nat. Catal.*, 2019, 2, 448–456.
- 92 G. Henkelman and H. Jónsson, *J. Chem. Phys.*, 2000, **113**, 9978–9985.
- 93 G. Henkelman, B. P. Uberuaga and H. Jónsson, *J. Chem. Phys.*, 2000, **113**, 9901–9904.
- 94 P. Xiao, D. Sheppard, J. Rogal and G. Henkelman, *J. Chem. Phys.*, 2014, **140**, 174104.
- 95 J. Hu, C. Zhang, L. Jiang, H. Lin, Y. An, D. Zhou, M. K. H. Leung and S. Yang, *Joule*, 2017, 1, 383–393.
- 96 Y. Xie, J. Cai, Y. Wu, Y. Zang, X. Zheng, J. Ye, P. Cui, S. Niu, Y. Liu, J. Zhu, X. Liu, G. Wang and Y. Qian, Adv. Mater., 2019, 31, 1807780.
- 97 Z. Lu, W. Xu, W. Zhu, Q. Yang, X. Lei, J. Liu, Y. Li, X. Sun and X. Duan, *Chem. Commun.*, 2014, **50**, 6479–6482.
- 98 T. Kou, S. Wang, J. L. Hauser, M. Chen, S. R. J. Oliver, Y. Ye, J. Guo and Y. Li, *ACS Energy Lett.*, 2019, 4, 622–628.
- 99 X. Yu, J. Zhao, L.-R. Zheng, Y. Tong, M. Zhang, G. Xu, C. Li, J. Ma and G. Shi, ACS Energy Lett., 2018, 3, 237–244.
- 100 H. Jiang, Y. Lin, B. Chen, Y. Zhang, H. Liu, X. Duan, D. Chen and L. Song, *Mater. Today*, 2018, **21**, 602–610.
- 101 M. Sheng, B. Jiang, B. Wu, F. Liao, X. Fan, H. Lin, Y. Li, Y. Lifshitz, S.-T. Lee and M. Shao, ACS Nano, 2019, 13, 2786–2794.
- 102 C.-T. Dinh, A. Jain, F. P. G. de Arquer, P. De Luna, J. Li, N. Wang, X. Zheng, J. Cai, B. Z. Gregory, O. Voznyy, B. Zhang, M. Liu, D. Sinton, E. J. Crumlin and E. H. Sargent, *Nat. Energy*, 2019, 4, 107–114.

- 103 M. G. Evans and M. Polanyi, *Trans. Faraday Soc.*, 1938, 34, 11–24.
- 104 R. P. Bell and C. N. Hinshelwood, *Proc. R. Soc. London, Ser. A*, 1936, **154**, 414–429.
- 105 T. Bligaard, J. K. Nørskov, S. Dahl, J. Matthiesen, C. H. Christensen and J. Sehested, *J. Catal.*, 2004, 224, 206–217.
- 106 Y. Li, H. Wang, L. Xie, Y. Liang, G. Hong and H. Dai, J. Am. Chem. Soc., 2011, 133, 7296–7299.
- 107 Y. Gong, L. Wang, H. Xiong, M. Shao, L. Xu, A. Xie, S. Zhuang, Y. Tang, X. Yang, Y. Chen and P. Wan, J. Mater. Chem. A, 2019, 7, 13671–13678.
- 108 K. Xiong, L. Li, L. Zhang, W. Ding, L. Peng, Y. Wang, S. Chen, S. Tan and Z. Wei, *J. Mater. Chem. A*, 2015, 3, 1863–1867.
- 109 D. Voiry, R. Fullon, J. Yang, C. de Carvalho Castro e Silva,
  R. Kappera, I. Bozkurt, D. Kaplan, M. J. Lagos,
  P. E. Batson, G. Gupta, A. D. Mohite, L. Dong, D. Er,
  V. B. Shenoy, T. Asefa and M. Chhowalla, *Nat. Mater.*,
  2016, 15, 1003-1009.
- 110 Y. Wang, L. Liu, X. Zhang, F. Yan, C. Zhu and Y. Chen, J. Mater. Chem. A, 2019, 7, 22412–22419.
- 111 R. Patil, V. Juvekar and U. Nalage, 2017, arXiv:1712.07382.
- 112 D. Kiuchi, H. Matsushima, Y. Fukunaka and K. Kuribayashi, J. Electrochem. Soc., 2006, 153, E138–E143.
- 113 M. Wang, Z. Wang, X. Gong and Z. Guo, Renewable Sustainable Energy Rev., 2014, 29, 573–588.
- 114 K. Qian, Z. D. Chen and J. J. J. Chen, *J. Appl. Electrochem.*, 1998, **28**, 1141–1145.
- 115 S. Geiger, O. Kasian, M. Ledendecker, E. Pizzutilo, A. M. Mingers, W. T. Fu, O. Diaz-Morales, Z. Li, T. Oellers, L. Fruchter, A. Ludwig, K. J. J. Mayrhofer, M. T. M. Koper and S. Cherevko, *Nat. Catal.*, 2018, 1, 508– 515.
- 116 N. Artrith and A. M. Kolpak, *Comput. Mater. Sci.*, 2015, **110**, 20–28.
- 117 K. J. J. Mayrhofer, S. J. Ashton, J. C. Meier, G. K. H. Wiberg, M. Hanzlik and M. Arenz, *J. Power Sources*, 2008, **185**, 734–739.
- 118 K. J. J. Mayrhofer, J. C. Meier, S. J. Ashton, G. K. H. Wiberg, F. Kraus, M. Hanzlik and M. Arenz, *Electrochem. Commun.*, 2008, **10**, 1144–1147.
- 119 M. J. N. Pourbaix, *Atlas of electrochemical equilibria in aqueous solution*, National Association of Corrosion, Houston, 1974.
- 120 F. J. Perez-Alonso, C. F. Elkjær, S. S. Shim, B. L. Abrams, I. E. Stephens and I. B. Chorkendorff, *J. Power Sources*, 2011, **196**, 6085–6091.
- 121 K. Schlögl, K. J. J. Mayrhofer, M. Hanzlik and M. Arenz, *J. Electroanal. Chem.*, 2011, **662**, 355–360.
- 122 Y. Shao-Horn, W. C. Sheng, S. Chen, P. J. Ferreira,E. F. Holby and D. Morgan, *Top. Catal.*, 2007, 46, 285–305.
- 123 K. Hartl, M. Hanzlik and M. Arenz, *Energy Environ. Sci.*, 2011, 4, 234–238.
- 124 H. Schulenburg, B. Schwanitz, N. Linse, G. G. Scherer, A. Wokaun, J. Krbanjevic, R. Grothausmann and I. Manke, *J. Phys. Chem. C*, 2011, **115**, 14236–14243.

- 125 M. M. Mench, E. C. Kumbur and T. N. Veziroglu, *Polymer Electrolyte Fuel Cell Degradation*, Academic Press, 2011.
- 126 M. Ma, K. Liu, J. Shen, R. Kas and W. A. Smith, *ACS Energy Lett.*, 2018, 3, 1301–1306.
- 127 K. Hu, T. Ohto, L. Chen, J. Han, M. Wakisaka, Y. Nagata, J.-i. Fujita and Y. Ito, ACS Energy Lett., 2018, 3, 1539–1544.
- 128 M. Ledendecker, J. S. Mondschein, O. Kasian, S. Geiger, D. Göhl, M. Schalenbach, A. Zeradjanin, S. Cherevko, R. E. Schaak and K. Mayrhofer, *Angew. Chem., Int. Ed.*, 2017, 56, 9767–9771.
- 129 J. Bonde, P. G. Moses, T. F. Jaramillo, J. K. Nørskov and I. Chorkendorff, *Faraday Discuss.*, 2009, **140**, 219–231.
- 130 D. Voiry, M. Salehi, R. Silva, T. Fujita, M. Chen, T. Asefa, V. B. Shenoy, G. Eda and M. Chhowalla, *Nano Lett.*, 2013, 13, 6222–6227.
- 131 C. Tsai, H. Li, S. Park, J. Park, H. S. Han, J. K. Nørskov, X. Zheng and F. Abild-Pedersen, *Nat. Commun.*, 2017, 8, 15113.
- 132 J. Hong, Z. Hu, M. Probert, K. Li, D. Lv, X. Yang, L. Gu, N. Mao, Q. Feng, L. Xie, J. Zhang, D. Wu, Z. Zhang, C. Jin, W. Ji, X. Zhang, J. Yuan and Z. Zhang, *Nat. Commun.*, 2015, 6, 6293.
- 133 C. G. Morales-Guio and X. Hu, Acc. Chem. Res., 2014, 47, 2671–2681.
- 134 H. Vrubel and X. Hu, ACS Catal., 2013, 3, 2002-2011.
- 135 D. Merki, S. Fierro, H. Vrubel and X. Hu, *Chem. Sci.*, 2011, 2, 1262–1267.
- 136 Y. Zheng, Y. Jiao, L. H. Li, T. Xing, Y. Chen, M. Jaroniec and S. Z. Qiao, *ACS Nano*, 2014, **8**, 5290–5296.
- 137 C. Hu and L. Dai, Adv. Mater., 2017, 29, 1604942.
- 138 L. Zhang, J. Xiao, H. Wang and M. Shao, *ACS Catal.*, 2017, 7, 7855–7865.
- 139 Y. Jiao, Y. Zheng, K. Davey and S.-Z. Qiao, *Nat. Energy*, 2016, 1, 16130.
- 140 N. Cheng, S. Stambula, D. Wang, M. N. Banis, J. Liu, A. Riese, B. Xiao, R. Li, T.-K. Sham, L.-M. Liu, G. A. Botton and X. Sun, *Nat. Commun.*, 2016, 7, 13638.
- 141 J. Deng, H. Li, J. Xiao, Y. Tu, D. Deng, H. Yang, H. Tian, J. Li, P. Ren and X. Bao, *Energy Environ. Sci.*, 2015, **8**, 1594–1601.
- 142 K. Jiang, B. Liu, M. Luo, S. Ning, M. Peng, Y. Zhao, Y.-R. Lu, T.-S. Chan, F. M. F. de Groot and Y. Tan, *Nat. Commun.*, 2019, **10**, 1743.
- 143 J. Liu, M. Jiao, L. Lu, H. M. Barkholtz, Y. Li, Y. Wang, L. Jiang, Z. Wu, D.-j. Liu, L. Zhuang, C. Ma, J. Zeng, B. Zhang, D. Su, P. Song, W. Xing, W. Xu, Y. Wang, Z. Jiang and G. Sun, *Nat. Commun.*, 2017, 8, 15938.
- 144 X. X. Wang, D. A. Cullen, Y.-T. Pan, S. Hwang, M. Wang, Z. Feng, J. Wang, M. H. Engelhard, H. Zhang, Y. He, Y. Shao, D. Su, K. L. More, J. S. Spendelow and G. Wu, Adv. Mater., 2018, 30, 1706758.
- 145 C. Zhu, S. Fu, J. Song, Q. Shi, D. Su, M. H. Engelhard, X. Li, D. Xiao, D. Li, L. Estevez, D. Du and Y. Lin, *Small*, 2017, 13, 1603407.
- 146 M. Naguib, M. Kurtoglu, V. Presser, J. Lu, J. Niu, M. Heon, L. Hultman, Y. Gogotsi and M. W. Barsoum, *Adv. Mater.*, 2011, 23, 4248–4253.

- 147 T. Y. Ma, J. L. Cao, M. Jaroniec and S. Z. Qiao, *Angew. Chem., Int. Ed.*, 2016, 55, 1138–1142.
- 148 Q. Xue, Z. Pei, Y. Huang, M. Zhu, Z. Tang, H. Li, Y. Huang, N. Li, H. Zhang and C. Zhi, *J. Mater. Chem. A*, 2017, 5, 20818–20823
- 149 D. A. Kuznetsov, Z. Chen, P. V. Kumar, A. Tsoukalou, A. Kierzkowska, P. M. Abdala, O. V. Safonova, A. Fedorov and C. R. Müller, J. Am. Chem. Soc., 2019, 141, 17809–17816.
- 150 J. Zhang, Y. Zhao, X. Guo, C. Chen, C.-L. Dong, R.-S. Liu, C.-P. Han, Y. Li, Y. Gogotsi and G. Wang, *Nat. Catal.*, 2018, 1, 985–992.
- 151 A. D. Handoko, K. D. Fredrickson, B. Anasori, K. W. Convey, L. R. Johnson, Y. Gogotsi, A. Vojvodic and Z. W. Seh, ACS Appl. Energy Mater., 2018, 1, 173–180.
- 152 P. Li, J. Zhu, A. D. Handoko, R. Zhang, H. Wang, D. Legut, X. Wen, Z. Fu, Z. W. Seh and Q. Zhang, *J. Mater. Chem. A*, 2018, 6, 4271–4278.
- 153 A. D. Handoko, S. N. Steinmann and Z. W. Seh, *Nanoscale Horiz.*, 2019, 4, 809–827.
- 154 J. Di, C. Yan, A. D. Handoko, Z. W. Seh, H. Li and Z. Liu, *Mater. Today*, 2018, **21**, 749–770.
- 155 M. Gong, W. Zhou, M.-C. Tsai, J. Zhou, M. Guan, M.-C. Lin, B. Zhang, Y. Hu, D.-Y. Wang, J. Yang, S. J. Pennycook, B.-J. Hwang and H. Dai, *Nat. Commun.*, 2014, 5, 4695.
- 156 T. Zhang, M.-Y. Wu, D.-Y. Yan, J. Mao, H. Liu, W.-B. Hu, X.-W. Du, T. Ling and S.-Z. Qiao, *Nano Energy*, 2018, 43, 103–109.
- 157 X. Yan, L. Tian and X. Chen, *J. Power Sources*, 2015, **300**, 336–343.
- 158 T. Ling, T. Zhang, B. Ge, L. Han, L. Zheng, F. Lin, Z. Xu, W.-B. Hu, X.-W. Du, K. Davey and S.-Z. Qiao, *Adv. Mater.*, 2019, **31**, 1807771.
- 159 J. Wang, S. Mao, Z. Liu, Z. Wei, H. Wang, Y. Chen and Y. Wang, *ACS Appl. Mater. Interfaces*, 2017, **9**, 7139–7147.
- 160 L.-L. Feng, G. Yu, Y. Wu, G.-D. Li, H. Li, Y. Sun, T. Asefa, W. Chen and X. Zou, J. Am. Chem. Soc., 2015, 137, 14023–14026.
- 161 N. Jiang, Q. Tang, M. Sheng, B. You, D.-e. Jiang and Y. Sun, *Catal. Sci. Technol.*, 2016, **6**, 1077–1084.
- 162 A. Sivanantham, P. Ganesan and S. Shanmugam, *Adv. Funct. Mater.*, 2016, **26**, 4661–4672.
- 163 J. Li, P. K. Shen and Z. Tian, *Int. J. Hydrogen Energy*, 2017, 42, 7136–7142.
- 164 M. Yang, Y. Jiang, S. Liu, M. Zhang, Q. Guo, W. Shen, R. He, W. Su and M. Li, *Nanoscale*, 2019, **11**, 14016–14023.
- 165 Y. Xie, Y. Liu and Z. Yang, *Int. J. Hydrogen Energy*, 2020, 45, 6500–6507.
- 166 Y. Xia, W. Wu, H. Wang, S. Rao, F. Zhang and G. Zou, *Nanotechnology*, 2020, 31, 145401.
- 167 Y. Wan, Z. Zhang, X. Xu, Z. Zhang, P. Li, X. Fang, K. Zhang, K. Yuan, K. Liu, G. Ran, Y. Li, Y. Ye and L. Dai, *Nano Energy*, 2018, 51, 786–792.
- 168 J. Hu, B. Huang, C. Zhang, Z. Wang, Y. An, D. Zhou, H. Lin, M. K. H. Leung and S. Yang, *Energy Environ. Sci.*, 2017, **10**, 593–603.
- 169 Y. Tan, P. Liu, L. Chen, W. Cong, Y. Ito, J. Han, X. Guo, Z. Tang, T. Fujita, A. Hirata and M. W. Chen, *Adv. Mater.*, 2014, 26, 8023–8028.

- 170 Q. Xu, Y. Liu, H. Jiang, Y. Hu, H. Liu and C. Li, *Adv. Energy Mater.*, 2019, **9**, 1970004.
- 171 Y. Yin, J. Han, Y. Zhang, X. Zhang, P. Xu, Q. Yuan, L. Samad, X. Wang, Y. Wang, Z. Zhang, P. Zhang, X. Cao, B. Song and S. Jin, *J. Am. Chem. Soc.*, 2016, 138, 7965–7972.
- 172 P. Liu, J. Zhu, J. Zhang, P. Xi, K. Tao, D. Gao and D. Xue, *ACS Energy Lett.*, 2017, 2, 745–752.
- 173 H. Li, S. Chen, X. Jia, B. Xu, H. Lin, H. Yang, L. Song and X. Wang, *Nat. Commun.*, 2017, **8**, 15377.
- 174 Y. Yin, Y. Zhang, T. Gao, T. Yao, X. Zhang, J. Han, X. Wang, Z. Zhang, P. Xu, P. Zhang, X. Cao, B. Song and S. Jin, *Adv. Mater.*, 2017, 29, 1700311.
- 175 L. Najafi, S. Bellani, R. Oropesa-Nuñez, A. Ansaldo, M. Prato, A. E. Del Rio Castillo and F. Bonaccorso, Adv. Energy Mater., 2018, 8, 1703212.
- 176 D. Gao, B. Xia, C. Zhu, Y. Du, P. Xi, D. Xue, J. Ding and J. Wang, *J. Mater. Chem. A*, 2018, **6**, 510–515.
- 177 C. Tan, Z. Luo, A. Chaturvedi, Y. Cai, Y. Du, Y. Gong, Y. Huang, Z. Lai, X. Zhang, L. Zheng, X. Qi, M. H. Goh, J. Wang, S. Han, X.-J. Wu, L. Gu, C. Kloc and H. Zhang, Adv. Mater., 2018, 30, 1705509.
- 178 M. A. Lukowski, A. S. Daniel, C. R. English, F. Meng, A. Forticaux, R. J. Hamers and S. Jin, *Energy Environ. Sci.*, 2014, 7, 2608–2613.
- 179 X. Shi, M. Fields, J. Park, J. M. McEnaney, H. Yan, Y. Zhang, C. Tsai, T. F. Jaramillo, R. Sinclair, J. K. Nørskov and X. Zheng, *Energy Environ. Sci.*, 2018, **11**, 2270–2277.
- 180 Y. Chen, S. Xu, Y. Li, R. J. Jacob, Y. Kuang, B. Liu, Y. Wang, G. Pastel, L. G. Salamanca-Riba, M. R. Zachariah and L. Hu, *Adv. Energy Mater.*, 2017, 7, 1700482.
- 181 V.-T. Nguyen, P. A. Le, Y.-C. Hsu and K.-H. Wei, *ACS Appl. Mater. Interfaces*, 2020, **12**, 11533–11542.
- 182 Y. Yang, K. Zhang, H. Lin, X. Li, H. C. Chan, L. Yang and Q. Gao, *ACS Catal.*, 2017, 7, 2357–2366.
- 183 J. Miao, F.-X. Xiao, H. B. Yang, S. Y. Khoo, J. Chen, Z. Fan, Y.-Y. Hsu, H. M. Chen, H. Zhang and B. Liu, *Sci. Adv.*, 2015, 1, e1500259.
- 184 S. Piontek, C. Andronescu, A. Zaichenko, B. Konkena, K. junge Puring, B. Marler, H. Antoni, I. Sinev, M. Muhler, D. Mollenhauer, B. Roldan Cuenya, W. Schuhmann and U.-P. Apfel, ACS Catal., 2018, 8, 987–996.
- 185 J. Yu, W.-J. Li, H. Zhang, F. Zhou, R. Li, C.-Y. Xu, L. Zhou, H. Zhong and J. Wang, *Nano Energy*, 2019, 57, 222–229.
- 186 Y. Ito, W. Cong, T. Fujita, Z. Tang and M. Chen, *Angew. Chem.*, *Int. Ed.*, 2015, **54**, 2131–2136.
- 187 T. Li, D. Tang, Z. Cui, B. Cai, D. Li, Q. Chen and C. Li, *Electrocatalysis*, 2018, 9, 573–581.
- 188 K. Qu, Y. Zheng, Y. Jiao, X. Zhang, S. Dai and S.-Z. Qiao, *Adv. Energy Mater.*, 2017, 7, 1602068.
- 189 J. Zhang, L. Qu, G. Shi, J. Liu, J. Chen and L. Dai, *Angew. Chem.*, *Int. Ed.*, 2016, 55, 2230–2234.
- 190 Y. Zhao, F. Zhao, X. Wang, C. Xu, Z. Zhang, G. Shi and L. Qu, *Angew. Chem., Int. Ed.*, 2014, **53**, 13934–13939.
- 191 M. Tavakkoli, N. Holmberg, R. Kronberg, H. Jiang, J. Sainio, E. I. Kauppinen, T. Kallio and K. Laasonen, *ACS Catal.*, 2017, 7, 3121–3130.

- 192 L. Zhang, L. Han, H. Liu, X. Liu and J. Luo, Angew. Chem., Int. Ed., 2017, 56, 13694-13698.
- 193 Y. Qu, B. Chen, Z. Li, X. Duan, L. Wang, Y. Lin, T. Yuan, F. Zhou, Y. Hu, Z. Yang, C. Zhao, J. Wang, C. Zhao, Y. Hu, G. Wu, Q. Zhang, Q. Xu, B. Liu, P. Gao, R. You, W. Huang, L. Zheng, L. Gu, Y. Wu and Y. Li, J. Am. Chem. Soc., 2019, 141, 4505-4509.
- 194 H. Zhang, P. An, W. Zhou, B. Y. Guan, P. Zhang, J. Dong and X. W. Lou, Sci. Adv., 2018, 4, eaao6657.
- 195 W. Liu, Q. Xu, P. Yan, J. Chen, Y. Du, S. Chu and J. Wang, ChemCatChem, 2018, 10, 946-950.
- 196 S. Ye, F. Luo, Q. Zhang, P. Zhang, T. Xu, Q. Wang, D. He, L. Guo, Y. Zhang, C. He, X. Ouyang, M. Gu, J. Liu and X. Sun, Energy Environ. Sci., 2019, 12, 1000-1007.
- 197 M. Li, K. Duanmu, C. Wan, T. Cheng, L. Zhang, S. Dai, W. Chen, Z. Zhao, P. Li, H. Fei, Y. Zhu, R. Yu, J. Luo, K. Zang, Z. Lin, M. Ding, J. Huang, H. Sun, J. Guo, X. Pan, W. A. Goddard, P. Sautet, Y. Huang and X. Duan, Nat. Catal., 2019, 2, 495-503.
- 198 Z. Luo, Y. Ouyang, H. Zhang, M. Xiao, J. Ge, Z. Jiang, J. Wang, D. Tang, X. Cao, C. Liu and W. Xing, Nat. Commun., 2018, 9, 2120.
- 199 T. Chao, X. Luo, W. Chen, B. Jiang, J. Ge, Y. Lin, G. Wu, X. Wang, Y. Hu, Z. Zhuang, Y. Wu, X. Hong and Y. Li, Angew. Chem., Int. Ed., 2017, 56, 16047-16051.
- 200 J. Yang, B. Chen, X. Liu, W. Liu, Z. Li, J. Dong, W. Chen, W. Yan, T. Yao, X. Duan, Y. Wu and Y. Li, Angew. Chem., Int. Ed., 2018, 57, 9495-9500.
- 201 S. Yuan, Z. Pu, H. Zhou, J. Yu, I. S. Amiinu, J. Zhu, Q. Liang, J. Yang, D. He, Z. Hu, G. Van Tendeloo and S. Mu, Nano Energy, 2019, 59, 472-480.
- 202 L. Zhang, R. Si, H. Liu, N. Chen, Q. Wang, K. Adair, Z. Wang, J. Chen, Z. Song, J. Li, M. N. Banis, R. Li, T.-K. Sham, M. Gu, L.-M. Liu, G. A. Botton and X. Sun, Nat. Commun., 2019, 10, 4936.
- 203 Y. Xue, B. Huang, Y. Yi, Y. Guo, Z. Zuo, Y. Li, Z. Jia, H. Liu and Y. Li, Nat. Commun., 2018, 9, 1460.
- 204 L. Fan, P. F. Liu, X. Yan, L. Gu, Z. Z. Yang, H. G. Yang, S. Qiu and X. Yao, Nat. Commun., 2016, 7, 10667.
- 205 H. Fei, J. Dong, M. J. Arellano-Jiménez, G. Ye, N. Dong Kim, E. L. G. Samuel, Z. Peng, Z. Zhu, F. Qin, J. Bao, M. J. Yacaman, P. M. Ajayan, D. Chen and J. M. Tour, Nat. Commun., 2015, 6, 8668.
- 206 L. Cao, Q. Luo, W. Liu, Y. Liu, Y. Liu, Y. Cao, W. Zhang, Y. Wu, J. Yang, T. Yao and S. Wei, Nat. Catal., 2019, 2, 134-141.
- 207 J.-D. Yi, R. Xu, G.-L. Chai, T. Zhang, K. Zang, B. Nan, H. Lin, Y.-L. Liang, J. Lv, J. Luo, R. Si, Y.-B. Huang and R. Cao, J. Mater. Chem. A, 2019, 7, 1252-1259.
- 208 W. Chen, J. Pei, C.-T. He, J. Wan, H. Ren, Y. Zhu, Y. Wang, J. Dong, S. Tian, W.-C. Cheong, S. Lu, L. Zheng, X. Zheng, W. Yan, Z. Zhuang, C. Chen, Q. Peng, D. Wang and Y. Li, Angew. Chem., Int. Ed., 2017, 56, 16086-16090.
- 209 W. Chen, J. Pei, C.-T. He, J. Wan, H. Ren, Y. Wang, J. Dong, K. Wu, W.-C. Cheong, J. Mao, X. Zheng, W. Yan, Z. Zhuang, C. Chen, Q. Peng, D. Wang and Y. Li, Adv. Mater., 2018, 30, 1800396.

- 210 S. Li, P. Tuo, J. Xie, X. Zhang, J. Xu, J. Bao, B. Pan and Y. Xie, Nano Energy, 2018, 47, 512-518.
- 211 Y. Jiang, T. Sun, X. Xie, W. Jiang, J. Li, B. Tian and C. Su, ChemSusChem, 2019, 12, 1368-1373.
- 212 Y. Yoon, A. P. Tiwari, M. Lee, M. Choi, W. Song, J. Im, T. Zyung, H.-K. Jung, S. S. Lee, S. Jeon and K.-S. An, J. Mater. Chem. A, 2018, 6, 20869-20877.
- 213 W. Yuan, L. Cheng, Y. An, H. Wu, N. Yao, X. Fan and X. Guo, ACS Sustainable Chem. Eng., 2018, 6, 8976-8982.
- 214 C.-F. Du, X. Sun, H. Yu, Q. Liang, K. N. Dinh, Y. Zheng, Y. Luo, Z. Wang and Q. Yan, Adv. Sci., 2019, 6, 1900116.
- 215 Z. Li, Z. Qi, S. Wang, T. Ma, L. Zhou, Z. Wu, X. Luan, F.-Y. Lin, M. Chen, J. T. Miller, H. Xin, W. Huang and Y. Wu, Nano Lett., 2019, 19, 5102-5108.
- 216 Y. Yuan, H. Li, L. Wang, L. Zhang, D. Shi, Y. Hong and J. Sun, ACS Sustainable Chem. Eng., 2019, 7, 4266-4273.
- 217 J. Liang, C. Ding, J. Liu, T. Chen, W. Peng, Y. Li, F. Zhang and X. Fan, Nanoscale, 2019, 11, 10992-11000.
- 218 N. H. Attanayake, S. C. Abeyweera, A. C. Thenuwara, B. Anasori, Y. Gogotsi, Y. Sun and D. R. Strongin, J. Mater. Chem. A, 2018, 6, 16882-16889.
- 219 C.-F. Du, K. N. Dinh, Q. Liang, Y. Zheng, Y. Luo, J. Zhang and Q. Yan, Adv. Energy Mater., 2018, 8, 1801127.
- 220 X. Wu, Z. Wang, M. Yu, L. Xiu and J. Qiu, Adv. Mater., 2017, 29, 1607017.
- 221 L. Xiu, Z. Wang, M. Yu, X. Wu and J. Qiu, ACS Nano, 2018, 12, 8017-8028.
- 222 P. Charoen-amornkitt, T. Suzuki and S. Tsushima, Electrochim. Acta, 2017, 258, 433-441.
- 223 J. Scholz, M. Risch, K. A. Stoerzinger, G. Wartner, Y. Shao-Horn and C. Jooss, J. Phys. Chem. C, 2016, 120, 27746-27756.
- 224 C. C. L. McCrory, S. Jung, J. C. Peters and T. F. Jaramillo, J. Am. Chem. Soc., 2013, 135, 16977-16987.
- 225 Y. Yoon, B. Yan and Y. Surendranath, J. Am. Chem. Soc., 2018, 140, 2397-2400.
- 226 S. Jung, C. C. L. McCrory, I. M. Ferrer, J. C. Peters and T. F. Jaramillo, J. Mater. Chem. A, 2016, 4, 3068-3076.
- 227 B. M. Weckhuysen, Phys. Chem. Chem. Phys., 2003, 5, 4351-4360.
- 228 M. A. Bañares, Catal. Today, 2005, 100, 71-77.
- 229 C. Hu, Q. Ma, S.-F. Hung, Z.-N. Chen, D. Ou, B. Ren, H. M. Chen, G. Fu and N. Zheng, Chem, 2017, 3, 122-133.
- 230 N. Kornienko, J. Resasco, N. Becknell, C.-M. Jiang, Y.-S. Liu, K. Nie, X. Sun, J. Guo, S. R. Leone and P. Yang, J. Am. Chem. Soc., 2015, 137, 7448-7455.
- 231 H. G. S. Casalongue, J. D. Benck, C. Tsai, R. K. B. Karlsson, S. Kaya, M. L. Ng, L. G. M. Pettersson, F. Abild-Pedersen, J. K. Nørskov, H. Ogasawara, T. F. Jaramillo and A. Nilsson, J. Phys. Chem. C, 2014, 118, 29252-29259.
- 232 J. H. K. Pfisterer, Y. Liang, O. Schneider and A. S. Bandarenka, Nature, 2017, 549, 74-77.
- 233 A. J. R. Hensley, K. Ghale, C. Rieg, T. Dang, E. Anderst, F. Studt, C. T. Campbell, J.-S. McEwen and Y. Xu, J. Phys. Chem. C, 2017, 121, 4937-4945.

- 234 Y. Ihm, C. Park, J. Jakowski, J. R. Morris, J. H. Shim, Y.-H. Kim, B. G. Sumpter and M. Yoon, *J. Phys. Chem. C*, 2018, **122**, 26189–26195.
- 235 C. J. Cramer and D. G. Truhlar, *J. Am. Chem. Soc.*, 1991, **113**, 8305–8311.
- 236 J. Sun, A. Ruzsinszky and J. P. Perdew, *Phys. Rev. Lett.*, 2015, 115, 036402.
- 237 Y. Zhao, N. González-García and D. G. Truhlar, *J. Phys. Chem. A*, 2005, **109**, 2012–2018.
- 238 N. L. Nguyen, N. Colonna, A. Ferretti and N. Marzari, *Phys. Rev. X*, 2018, **8**, 021051.
- 239 J. Ma and L.-W. Wang, Sci. Rep., 2016, 6, 24924.
- 240 T. J. Smart, F. Wu, M. Govoni and Y. Ping, *Phys. Rev. Mater.*, 2018, 2, 124002.
- 241 G. Miceli, W. Chen, I. Reshetnyak and A. Pasquarello, *Phys. Rev. B*, 2018, **97**, 121112.
- 242 N. P. Brawand, M. Govoni, M. Vörös and G. Galli, *J. Chem. Theory Comput.*, 2017, **13**, 3318–3325.
- 243 H. Zheng, M. Govoni and G. Galli, *Phys. Rev. Mater.*, 2019, 3, 073803.
- 244 W. Chen, G. Miceli, G.-M. Rignanese and A. Pasquarello, *Phys. Rev. Mater.*, 2018, 2, 073803.
- 245 P. Liu, C. Franchini, M. Marsman and G. Kresse, *J. Phys.: Condens. Matter*, 2019, 32, 015502.
- 246 P. S. Schmidt and K. S. Thygesen, *J. Phys. Chem. C*, 2018, 122, 4381–4390.
- 247 C. A. Gaggioli, S. J. Stoneburner, C. J. Cramer and L. Gagliardi, ACS Catal., 2019, 9, 8481–8502.
- 248 T. Bligaard, R. M. Bullock, C. T. Campbell, J. G. Chen, B. C. Gates, R. J. Gorte, C. W. Jones, W. D. Jones, J. R. Kitchin and S. L. Scott, *ACS Catal.*, 2016, **6**, 2590–2602.

- 249 W. B. Schneider and A. A. Auer, Beilstein J. Nanotechnol., 2014. 5, 668–676.
- 250 Z. Wang, Y. Yang, D. L. Olmsted, M. Asta and B. B. Laird, *J. Chem. Phys.*, 2014, **141**, 184102.
- 251 R. E. Skyner, J. L. McDonagh, C. R. Groom, T. van Mourik and J. B. O. Mitchell, *Phys. Chem. Chem. Phys.*, 2015, 17, 6174–6191.
- 252 J. Zhang, H. Zhang, T. Wu, Q. Wang and D. van der Spoel, J. Chem. Theory Comput., 2017, 13, 1034–1043.
- 253 K. Mathew, R. Sundararaman, K. Letchworth-Weaver, T. A. Arias and R. G. Hennig, J. Chem. Phys., 2014, 140, 084106.
- 254 C. J. Cramer and D. G. Truhlar, *Chem. Rev.*, 1999, **99**, 2161–2200.
- 255 A. V. Marenich, R. M. Olson, C. P. Kelly, C. J. Cramer and D. G. Truhlar, J. Chem. Theory Comput., 2007, 3, 2011–2033.
- 256 A. Fortunelli and J. Tomasi, *Chem. Phys. Lett.*, 1994, **231**, 34–39.
- 257 O. Andreussi, I. Dabo and N. Marzari, J. Chem. Phys., 2012, 136, 064102.
- 258 C. Dupont, O. Andreussi and N. Marzari, *J. Chem. Phys.*, 2013, **139**, 214110.
- 259 T. Shinagawa and K. Takanabe, *J. Power Sources*, 2015, **287**, 465–471.
- 260 Y. Ping, R. Sundararaman and W. A. Goddard Iii, *Phys. Chem. Chem. Phys.*, 2015, 17, 30499–30509.
- 261 K. Schwarz, B. Xu, Y. Yan and R. Sundararaman, *Phys. Chem. Chem. Phys.*, 2016, **18**, 16216–16223.
- 262 M. A. Butler, R. D. Nasby and R. K. Quinn, *Solid State Commun.*, 1976, **19**, 1011–1014.